

# Classical Reaction Barriers in DFT: An Adiabatic-Connection Perspective

Andrew M. Wibowo-Teale,\* Bang C. Huynh, Trygve Helgaker,\* and David J. Tozer\*

Cite This: *J. Chem. Theory Comput.* 2025, 21, 124–137

Read Online

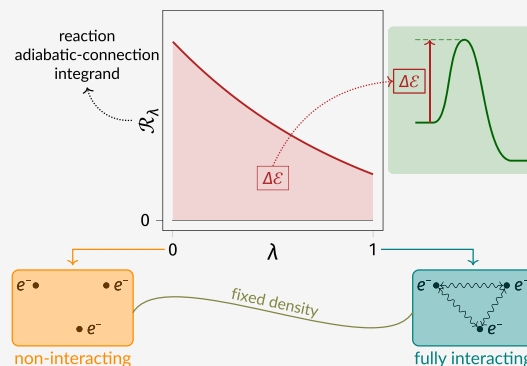
ACCESS |

Metrics & More

Article Recommendations

Supporting Information

**ABSTRACT:** Classical reaction barriers in density-functional theory are considered from the perspective of the density-fixed adiabatic connection. A ‘reaction adiabatic-connection integrand’,  $\mathcal{R}_\lambda$ , is introduced, where  $\lambda$  is the electron–electron interaction strength, for which  $\int_0^1 \mathcal{R}_\lambda d\lambda$  equals the barrier, meaning the barrier can be easily visualized as the area under a plot of  $\mathcal{R}_\lambda$  vs  $\lambda$ . For five chemical reactions, plots of reference  $\mathcal{R}_\lambda$ , calculated from Lieb maximizations at the coupled-cluster level of theory, are compared with approximate  $\mathcal{R}_\lambda$ , calculated from common exchange–correlation functionals using coordinate scaling, for coupled-cluster densities. The comparison provides a simple way to visualize and understand functional-driven errors and trends in barriers from approximate functionals, while allowing a clean separation of the role of exchange and correlation contributions to the barrier. Specifically, the accuracy of  $\mathcal{R}_0$  is determined entirely by the accuracy of the exchange functional, while the shape of  $\mathcal{R}_\lambda$  is determined entirely by the correlation functional. The results clearly illustrate why the optimal amount of exact (orbital) exchange in hybrid functionals differs between reactions, including forward and reverse directions in the same reaction, and hence why simply introducing larger amounts of exact exchange may not be a reliable approach for improving barriers. Instead, the shape of  $\mathcal{R}_\lambda$  must be captured more accurately through more accurate correlation functionals, and the numerical data presented may be useful for this purpose. Density-driven errors are then considered, and possible cancellation with functional-driven errors in barriers—noted in prior studies when Hartree–Fock densities are used—is illustrated from the perspective of  $\mathcal{R}_\lambda$ .



## 1. INTRODUCTION

Kohn–Sham density-functional theory<sup>1</sup> (DFT) is the most widely used electronic-structure method, achieving remarkable accuracy—considering its relatively low cost—for a broad range of properties and quantities.<sup>2–4</sup> The accuracy of a practical DFT calculation is governed by the accuracy of the exchange–correlation energy functional,  $E_{xc}[\rho]$ , where  $\rho$  is the electron density. Numerous density functional-approximations (DFAs) to this quantity have been proposed.

One chemical quantity that remains a particular challenge for DFAs, especially semilocal approximations, is the classical reaction barrier,

$$\Delta\mathcal{E} = \mathcal{E}^\ddagger - \sum_r n^r \mathcal{E}^r \quad (1)$$

where  $\mathcal{E}^\ddagger$  is the total energy (electronic and nuclear repulsion) of the transition state ( $\ddagger$ ) and the summation is over reactants ( $r$ ) with total energies,  $\mathcal{E}^r$ , weighted by their stoichiometries,  $n^r$ . We shall, hereafter, simply refer to it as a ‘barrier’. It is well established that DFAs often significantly underestimate barriers and this deficiency has been analyzed in terms of the one-electron self-interaction error<sup>5–18</sup> and many-electron self-interaction or delocalization errors.<sup>19–23</sup> A common approach

for improving the accuracy of barriers from DFAs is to increase the amount of exact (orbital) exchange,<sup>13,24</sup> to yield hybrid DFAs. Alternatively, the use of explicit self-interaction corrections has been explored.<sup>10,11,16–18,25,26</sup>

While the perspectives of self-interaction and delocalization errors give important insight into how errors in barriers arise, they do not distinguish clearly between the role of errors in the exchange and correlation components of  $E_{xc}[\rho]$ . The aim of the present work is to consider barriers in DFT from a new perspective, namely that of the density-fixed adiabatic connection,<sup>27–30</sup> which does clearly distinguish the effects of exchange and correlation. This approach, which connects the Kohn–Sham noninteracting electronic system ( $\lambda = 0$ ) with the physical interacting system ( $\lambda = 1$ ) through a series of partially interacting systems with electron–electron interaction strength,  $\lambda$ , with the same density, underpins many important aspects of

**Received:** August 8, 2024  
**Revised:** November 27, 2024  
**Accepted:** December 2, 2024  
**Published:** December 23, 2024



DFT, including hybrid functionals<sup>31</sup> and the perturbation theory of Görling and Levy.<sup>32</sup>

We commence in Section 2 by presenting the necessary theory and computational details. Starting from the Levy constrained-search variation principle,<sup>33</sup> we define the exchange–correlation integrand,  $\mathcal{W}_{xc,\lambda}[\rho]$ , the accurate calculation of which requires an accurate wave function for interaction strength  $\lambda$ . We then show how maximization of the Lieb functional<sup>34</sup> using a correlated electronic-structure method can yield such a wave function and hence an accurate reference  $\mathcal{W}_{xc,\lambda}[\rho]$ . We also describe how  $\mathcal{W}_{xc,\lambda}[\rho]$  can be determined for an arbitrary DFA by coordinate scaling.<sup>35–38</sup> We then describe how we compute Kohn–Sham barriers, and how they relate to  $\mathcal{W}_{xc,\lambda}[\rho]$ , and we distinguish between functional- and density-driven errors.<sup>39</sup>

In Section 3, we present plots of  $\mathcal{W}_{xc,\lambda}[\rho]$ , as a function of  $\lambda$ , for the reactants and transition state in a simple reaction, comparing accurate reference plots, determined from Lieb maximizations using coupled-cluster singles-doubles-perturbative-triples (CCSD(T)) wave functions,<sup>40</sup> with plots for common DFAs, determined using coordinate scaling for relaxed (Lagrangian) CCSD(T) densities. Consideration of the associated barriers leads us to define a ‘reaction adiabatic-connection integrand’,  $\mathcal{R}_\lambda$ , involving the difference between  $\mathcal{W}_{xc,\lambda}[\rho]$  of the transition state and reactants, whose integral between  $\lambda = 0$  and  $\lambda = 1$  equals the barrier.

In Section 4, plots of reference CCSD(T)  $\mathcal{R}_\lambda$ , as a function of  $\lambda$ , are compared with those from approximate DFAs for five chemical reactions, providing insight into the dependence on DFA, the role of exchange and correlation contributions, the effect of adding an amount of exact exchange to yield hybrid functionals, the differences between forward and reverse reactions, and the distinction between functional- and density-driven errors. Finally, some conclusions are presented in Section 5.

## 2. THEORY AND COMPUTATIONAL DETAILS

**2.1. Levy Constrained-Search Functional.** Consider an  $N$ -electron system with the Hamiltonian,

$$\hat{H}_1[v] = \hat{T} + \lambda\hat{W} + \sum_i v(\mathbf{r}_i) \quad (2)$$

where  $\hat{T}$  is the kinetic-energy operator,  $\hat{W}$  is the electron–electron repulsion operator, and  $v$  is the external potential. The ground-state electronic energy at a given interaction strength,  $\lambda \in [0, 1]$ , is given by the Rayleigh–Ritz variation principle as

$$E_\lambda[v] = \inf_{\Psi_\lambda \in \mathcal{U}_N} \langle \Psi_\lambda | \hat{H}_1[v] | \Psi_\lambda \rangle \quad (3)$$

where  $\mathcal{U}_N$  is the set of all  $L^2$ -normalized, antisymmetric  $N$ -electron wave functions with a finite kinetic energy. The ground-state energy in eq 3 is well-defined for all potentials  $v \in \chi^*$  with  $\chi^* = L^{3/2} + L^\infty$ , a vector space that includes all Coulomb potentials. A minimizing wave function may or may not exist in eq 3, depending on whether the external potential  $v$  supports an  $N$ -electron ground state.

Following Levy,<sup>33</sup> we may express the ground-state energy of eq 3 in the form

$$E_\lambda[v] = \inf_{\rho \in \mathcal{I}_N} [F_\lambda[\rho] + \int \rho(\mathbf{r})v(\mathbf{r})d\mathbf{r}] \quad (4)$$

where  $\mathcal{I}_N \subset \chi = L^3 \cap L^1$  is the set of all  $N$ -representable densities and

$$F_\lambda[\rho] = \min_{\Psi \rightarrow \rho} \langle \Psi | \hat{T} + \lambda\hat{W} | \Psi \rangle \quad (5)$$

is the constrained-search expression for the universal density functional. For each interaction strength  $\lambda$  and each  $\rho \in \mathcal{I}_N$ , one or more minimizing wave functions exist in the constrained search and we may therefore write the universal density functional as an expectation value

$$F_\lambda[\rho] = \langle \Psi_\lambda^\rho | \hat{T} + \lambda\hat{W} | \Psi_\lambda^\rho \rangle \quad (6)$$

where  $\Psi_\lambda^\rho$  is one of the minimizing wave functions of eq 5.

**2.2. Kohn–Sham Decomposition and Adiabatic Connection.** Differentiating eq 6 with respect to  $\lambda$  and applying the Hellmann–Feynman theorem, we arrive at the adiabatic-connection expression for the universal density functional,<sup>27–30</sup>

$$F_\lambda[\rho] = T_s[\rho] + \int_0^\lambda \langle \Psi_\mu^\rho | \hat{W} | \Psi_\mu^\rho \rangle d\mu \quad (7)$$

where  $T_s[\rho] = F_0[\rho]$  is the noninteracting kinetic energy functional. Introducing the classical Coulomb (Hartree) energy functional,  $E_J[\rho]$ , and the exchange–correlation integrand

$$\mathcal{W}_{xc,\lambda}[\rho] = \langle \Psi_\lambda^\rho | \hat{W} | \Psi_\lambda^\rho \rangle - E_J[\rho] \quad (8)$$

we obtain from eq 7 the Kohn–Sham decomposition of the universal density functional,<sup>1</sup>

$$F_\lambda[\rho] = T_s[\rho] + \lambda E_J[\rho] + E_{xc,\lambda}[\rho] \quad (9)$$

where the exchange–correlation energy at interaction strength  $\lambda$  is given by

$$E_{xc,\lambda}[\rho] = \int_0^\lambda \mathcal{W}_{xc,\mu}[\rho] d\mu \quad (10)$$

Evaluation of  $E_{xc,\lambda}[\rho]$  at  $\lambda = 1$  yields the familiar exchange–correlation energy of the interacting system,  $E_{xc}[\rho]$ . The exchange–correlation energy at interaction strength  $\lambda$  may be further decomposed into exchange and correlation energies

$$E_{xc,\lambda}[\rho] = \lambda E_x[\rho] + E_{c,\lambda}[\rho] \quad (11)$$

where the exchange energy,  $E_x[\rho]$ , is obtained by evaluating eq 8 at  $\lambda = 0$ , that is, using the noninteracting wave function,

$$E_x[\rho] = \mathcal{W}_{xc,0}[\rho] = \langle \Psi_0^\rho | \hat{W} | \Psi_0^\rho \rangle - E_J[\rho] \quad (12)$$

and the remainder,  $E_{c,\lambda}[\rho] = E_{xc,\lambda}[\rho] - \lambda E_x[\rho]$ , is the correlation energy at interaction strength  $\lambda$ ,

$$E_{c,\lambda}[\rho] = \int_0^\lambda (\mathcal{W}_{xc,\mu}[\rho] - E_x[\rho]) d\mu \quad (13)$$

Thus, while the exchange energy represents the (usually dominant) linear dependence of the exchange–correlation energy on the interaction strength, all (usually small) nonlinear dependence is contained in the correlation energy.

The exchange–correlation integrand,  $\mathcal{W}_{xc,\lambda}[\rho]$  in eq 8, is the central adiabatic-connection quantity in the present work. Our first task is to evaluate this quantity accurately, which requires us to compute  $\Psi_\lambda^\rho$  using high-precision quantum chemistry. This, in turn, requires a consideration of the Lieb functional and its maximization.<sup>34</sup>

**2.3. Lieb Functional.** The (constrained-search) universal density functional in eq 5 is not directly amenable to calculation.

There exists, however, an alternative formulation of the universal density functional, which is well suited to calculation and which yields the minimizing wave function  $\Psi_{\lambda}^{\rho}$ , thereby enabling the calculation of the desired  $\mathcal{W}_{\text{xc},\lambda}[\rho]$  in eq 8.

Noting that the ground-state electronic energy  $E_{\lambda}[v]$  is continuous and concave in the external potential, Lieb concluded that there exists a (convex) universal density functional  $\tilde{F}_{\lambda}[\rho]$  such that<sup>34</sup>

$$\tilde{F}_{\lambda}[\rho] = \sup_{v \in \mathcal{X}^*} [E_{\lambda}[v] - \int \rho(\mathbf{r})v(\mathbf{r})d\mathbf{r}] \quad (14)$$

$$E_{\lambda}[v] = \inf_{\rho \in \mathcal{X}} [\tilde{F}_{\lambda}[\rho] + \int \rho(\mathbf{r})v(\mathbf{r})d\mathbf{r}] \quad (15)$$

where  $\tilde{F}_{\lambda}[\rho] \leq F_{\lambda}[\rho]$  for each  $\rho \in \mathcal{I}_N$ , with equality for all pure-state  $v$ -representable densities.<sup>34</sup> We note in passing that, if the constrained search<sup>33</sup> in eq 5 is extended to include also a search over mixed states, then full equality with the Lieb functional is obtained.<sup>34</sup> Note also that, if  $E_{\lambda}[v]$  of eq 3 is substituted in eq 14, then the external potential of the Lieb functional plays the role of a Lagrange multiplier in an unconstrained minimax optimization of the universal density functional.

For a  $v$ -representable density  $\rho$ , the supremum in the Lieb functional of eq 14 can be attained and there exists a potential  $v_{\lambda}^{\rho}$  such that

$$\tilde{F}_{\lambda}[\rho] = E_{\lambda}[v_{\lambda}^{\rho}] - \int \rho(\mathbf{r})v_{\lambda}^{\rho}(\mathbf{r})d\mathbf{r} \quad (16)$$

The optimization to yield the maximizing potential  $v_{\lambda}^{\rho}$  can be carried out practically<sup>41–44</sup> by choosing a correlated electronic-structure method to calculate  $E_{\lambda}[v]$  in eq 14 and setting the density  $\rho$  in eq 14 equal to the interacting density from that electronic-structure method, for all  $\lambda \in [0, 1]$ . Once the maximizing potential is obtained, the wave function  $\Psi_{\lambda}^{\rho}$ , required for the evaluation of  $\mathcal{W}_{\text{xc},\lambda}[\rho]$  in eq 8, can be obtained directly from the calculation of  $E_{\lambda}[v]$ .

**2.4. Reference  $\mathcal{W}_{\text{xc},\lambda}[\rho]$  from Lieb Maximizations.** The potential in eq 16 depends explicitly on  $\lambda$  and can be decomposed in the manner used in Kohn–Sham theory,

$$v_{\lambda}^{\rho}(\mathbf{r}) = v_{\text{ext}}(\mathbf{r}) + (1 - \lambda)v_j(\mathbf{r}) + (1 - \lambda)v_x(\mathbf{r}) + [v_{c,1}(\mathbf{r}) - v_{c,\lambda}(\mathbf{r})] \quad (17)$$

where  $v_{\text{ext}}(\mathbf{r})$  is the external potential due to the nuclei,  $v_j(\mathbf{r})$  is the Coulomb potential from density  $\rho$ ,  $v_x(\mathbf{r})$  is the exchange potential, and the final term corresponds to the difference between the full correlation potential  $v_{c,1}(\mathbf{r})$  and that at the interaction strength under consideration,  $v_{c,\lambda}(\mathbf{r})$ .

To facilitate the optimization in eq 14 with respect to the potential for a given density  $\rho$ , the potential is expanded in a Gaussian basis as proposed by Wu and Yang,<sup>42,45</sup>

$$v_{\mathbf{b},\lambda}(\mathbf{r}) = v_{\text{ext}}(\mathbf{r}) + (1 - \lambda)v_j(\mathbf{r}) + (1 - \lambda)v_{\text{ref}}(\mathbf{r}) + \sum_t b_t g_t(\mathbf{r}) \quad (18)$$

in which  $v_{\text{ref}}(\mathbf{r})$  is a reference potential evaluated on  $\rho$ , which ensures that  $v_{\mathbf{b},\lambda}(\mathbf{r})$  has the correct asymptotic behavior, while  $g_t$  are a set of Gaussian functions with expansion coefficients  $b_t$  to be determined. The form of the reference potential employed in this work is that of the localized Hartree–Fock potential,<sup>46</sup> corrected at long-range by an approximate Fukui potential.<sup>47</sup>

The details of the construction of the reference potential are given in ref 48.

With the parametrization of the potential in eq 18, the universal density functional in eq 14 can be calculated by maximizing the objective function,

$$G_{\lambda,\rho}[\mathbf{b}] = E_{\lambda}[v_{\mathbf{b},\lambda}] - \int \rho(\mathbf{r})v_{\mathbf{b},\lambda}(\mathbf{r})d\mathbf{r} \quad (19)$$

with respect to variations in the potential-basis coefficients  $\mathbf{b}$ . The gradient of eq 19 with respect to these coefficients is given by<sup>42</sup>

$$\frac{\partial G_{\lambda,\rho}[\mathbf{b}]}{\partial b_t} = \int [\rho_{\mathbf{b},\lambda}(\mathbf{r}) - \rho(\mathbf{r})]g_t(\mathbf{r})d\mathbf{r} \quad (20)$$

while the second derivative of the objective function with respect to the potential-basis coefficients is given by<sup>42</sup>

$$\frac{\partial^2 G_{\lambda,\rho}[\mathbf{b}]}{\partial b_t \partial b_u} = \iint g_t(\mathbf{r})g_u(\mathbf{r}') \frac{\delta \rho_{\mathbf{b},\lambda}(\mathbf{r})}{\delta v_{\mathbf{b},\lambda}(\mathbf{r}')} d\mathbf{r} d\mathbf{r}' \quad (21)$$

At the maximizing potential  $v_{\lambda}^{\rho}$ , the iterating density  $\rho_{\mathbf{b},\lambda}$  becomes identical to the input density  $\rho$ .

In this work, the objective function is maximized by an approximate Newton approach<sup>49</sup> combined with GDIIS<sup>50</sup> as implemented in the QUEST program.<sup>51</sup> This is a second-order optimization algorithm in which the Hessian is approximated by the noninteracting Hessian, given by eq 21 at  $\lambda = 0$ .<sup>49</sup> Initially, the basis coefficients of the potential are updated at each iteration using a backtracking line search and  $E_{\lambda}$  is evaluated with the corresponding potential  $v_{\mathbf{b},\lambda}$ , yielding the energy and iterating density  $\rho_{\mathbf{b},\lambda}$  from which the objective function eq 19, gradient eq 20, and approximate Hessian are constructed. When the Euclidean norm of the gradient in eq 20 falls below  $10^{-4}$  a.u., the GDIIS algorithm is used to achieve convergence to a final gradient norm of  $10^{-8}$  a.u. The use of GDIIS acceleration is discussed in Appendix A and ensures that very tight convergence can be achieved at all interaction strengths. At each step, the approximate Hessian is regularized using the smoothing norm procedure of ref 52, with a regularisation parameter of  $10^{-5}$  a.u.

All Lieb maximizations in this work are carried out at the CCSD(T)<sup>40</sup> level of theory in the cc-pCVTZ basis<sup>53–56</sup> for  $\lambda \in [0, 1]$ . See the Supporting Information for further details. The same basis set is used for all calculations throughout this work. The relaxed (Lagrangian) CCSD(T) density<sup>57–59</sup> and the wave function  $\Psi_{\lambda}^{\rho}$  from the  $\lambda$ -interacting CCSD(T) calculation in the Lieb maximization are used to calculate  $\mathcal{W}_{\text{xc},\lambda}[\rho]$  in eq 8. We shall use this as our reference  $\mathcal{W}_{\text{xc},\lambda}[\rho]$  throughout this work.

**2.5.  $\mathcal{W}_{\text{xc},\lambda}[\rho]$  from Exchange–Correlation Energy Functionals.** For any exchange–correlation functional  $E_{\text{xc}}[\rho]$ —exact or approximate—the corresponding integrand  $\mathcal{W}_{\text{xc},\lambda}[\rho]$  can be determined from coordinate scaling,<sup>35–38</sup>

$$\mathcal{W}_{\text{xc},\lambda}[\rho] = \frac{\partial}{\partial \lambda} \lambda^2 E_{\text{xc}}[\rho_{1/\lambda}] \quad (22)$$

where  $\rho_{1/\lambda}$  is the coordinate-scaled density,

$$\rho_{1/\lambda}(\mathbf{r}) = \lambda^{-3} \rho(\mathbf{r}/\lambda) \quad (23)$$

Partitioning  $E_{\text{xc}}[\rho]$  into exchange and correlation functionals, and using the fact that the exchange functional satisfies the coordinate-scaling condition,<sup>35</sup>

$$E_{\text{x}}[\rho_{1/\lambda}] = \lambda^{-1} E_{\text{x}}[\rho] \quad (24)$$

we obtain

$$\mathcal{W}_{\text{xc},\lambda}[\rho] = E_{\text{x}}[\rho] + 2\lambda E_{\text{c}}[\rho_{1/\lambda}] + \lambda^2 \frac{\partial E_{\text{c}}[\rho_{1/\lambda}]}{\partial \lambda} \quad (25)$$

The exchange contribution to  $\mathcal{W}_{\text{xc},\lambda}[\rho]$  is therefore constant in  $\lambda$  and equal to the exchange energy, in agreement with eqs 10–12. Any deviation from constancy in  $\mathcal{W}_{\text{xc},\lambda}[\rho]$  reflects the effect of electron correlation and arises from second- and higher-order dependence of the correlation energy on  $\lambda$ .

We use eq 25 to determine  $\mathcal{W}_{\text{xc},\lambda}[\rho]$  for DFA energy functionals. The coordinate-scaled correlation functional  $E_{\text{c}}[\rho_{1/\lambda}]$  can be readily evaluated for a given DFA using the scheme described in ref 60. In this approach, the ingredients defining the functional are coordinate scaled to evaluate  $E_{\text{c}}[\rho_{1/\lambda}]$ ; expressions for these quantities may be found in eqs 49–53 of ref 60. Some care is required to ensure accurate numerical integration of the scaled quantities as  $\lambda$  approaches zero. In practice, we use a relatively fine numerical quadrature grid consisting of the order-41 Lebedev angular grid and a radial component constructed using the scheme of Lindh, Malmqvist, and Gagliardi<sup>61</sup> with a relative error threshold of  $10^{-10}$  a.u. Once  $E_{\text{c}}[\rho_{1/\lambda}]$  has been determined, the  $\lambda$ -derivative in the final term of eq 25 is evaluated by a simple forward finite difference with a step size of  $10^{-6}$  in  $\lambda$ .

This procedure has been implemented in the QUEST program<sup>51</sup> and is available for all DFAs in the XCFun<sup>62</sup> or LibXC<sup>63</sup> libraries. For a given DFA, the implementation allows eq 25 to be evaluated for any available density; we consider the self-consistent Kohn–Sham density of the DFA under study, the Hartree–Fock density, and the reference CCSD(T) density. For meta-GGA functionals and functionals containing exact (orbital) exchange, the evaluation of eq 25 requires a knowledge of the orbitals corresponding to the density. For the Kohn–Sham and Hartree–Fock densities, we use the orbitals from standard self-consistent field calculations. For the reference CCSD(T) density, the orbitals are obtained from a CCSD(T) Lieb maximization, as described in Section 2.4, at  $\lambda = 0$ . The optimizing potential of eq 17 is, in this case, the Kohn–Sham effective potential  $v_{\text{s}}$ , yielding Kohn–Sham orbitals and orbital energies consistent with the CCSD(T) density.

**2.6. Kohn–Sham Barriers.** Next, consider Kohn–Sham barriers and how they relate to  $\mathcal{W}_{\text{xc},\lambda}[\rho]$ . In the Kohn–Sham decomposition,<sup>1</sup> the total energy at interaction strength  $\lambda$  takes the form

$$\mathcal{E}_{\lambda} = T_{\text{s}}[\{\varphi_i\}] + E_{\text{ext}}[\rho] + \lambda E_{\text{J}}[\rho] + E_{\text{xc},\lambda}[\rho] + E_{\text{nn}} \quad (26)$$

where  $T_{\text{s}}[\{\varphi_i\}]$  is the noninteracting kinetic energy calculated from the occupied Kohn–Sham orbitals  $\varphi_i$ ,  $E_{\text{ext}}[\rho] = \int \rho(\mathbf{r})v(\mathbf{r})\text{d}\mathbf{r}$  is the interaction energy between the density and the external potential, and  $E_{\text{nn}}$  is the nuclear repulsion energy, which depends only on the nuclear coordinates and charges. Inserting eq 26 into eq 1 and using eq 10, the barrier at interaction strength  $\lambda$  can be written as

$$\Delta\mathcal{E}_{\lambda} = C_{\text{R}} + \int_0^{\lambda} \mathcal{R}_{\text{Jxc},\mu} \text{d}\mu \quad (27)$$

where the first term contains the Kohn–Sham contributions to the barrier that are independent of the interaction strength,

$$C_{\text{R}} = (T_{\text{s}}[\{\varphi_i^{\ddagger}\}] + E_{\text{ext}}^{\ddagger}[\rho^{\ddagger}] + E_{\text{nn}}^{\ddagger}) - \sum_{\text{r}} n^{\text{r}}(T_{\text{s}}[\{\varphi_i^{\text{r}}\}] + E_{\text{ext}}^{\text{r}}[\rho^{\text{r}}] + E_{\text{nn}}^{\text{r}}) \quad (28)$$

while the second term contains the exchange–correlation and Coulomb contributions to the barrier, calculated by interaction-strength integration over the integrand,

$$\mathcal{R}_{\text{Jxc},\lambda} = \mathcal{W}_{\text{xc},\lambda}[\rho^{\ddagger}] + E_{\text{J}}[\rho^{\ddagger}] - \sum_{\text{r}} n^{\text{r}}(\mathcal{W}_{\text{xc},\lambda}[\rho^{\text{r}}] + E_{\text{J}}[\rho^{\text{r}}]) \quad (29)$$

Note that the use of two superscripts in  $E_{\text{ext}}^{\ddagger}[\rho^{\ddagger}]$  and  $E_{\text{ext}}^{\text{r}}[\rho^{\text{r}}]$  in eq 28 emphasizes that both the density and external potential depend on the molecular structure.

For a given DFA, we use the QUEST program<sup>51</sup> to evaluate the barrier in eq 27 for the self-consistent Kohn–Sham density of the DFA under study, the Hartree–Fock density and the reference CCSD(T) density.

For the self-consistent Kohn–Sham density, the  $T_{\text{s}}$ ,  $E_{\text{ext}}$ , and  $E_{\text{J}}$  terms in eqs 28 and 29 are calculated directly from the self-consistent density and corresponding orbitals. The  $\mathcal{W}_{\text{xc},\lambda}[\rho]$  terms in eq 29 are evaluated for the self-consistent density, as described in Section 2.5, for  $\lambda \in [0, 1]$  in steps of 0.05. The integral in eq 27 is then evaluated numerically using these data. We have confirmed that, for the systems considered in this work, the physical barriers (eq 27 for  $\lambda = 1$ ) determined in this manner agree with the conventionally calculated DFA barriers to better than 0.1 kcal mol<sup>-1</sup>; the high accuracy follows from the fact that  $\mathcal{W}_{\text{xc},\lambda}[\rho]$  is a smooth function of  $\lambda$ .

For the Hartree–Fock density, exactly the same procedure is followed, except that the Hartree–Fock density and orbitals are used throughout, instead of self-consistent Kohn–Sham ones. For the reference CCSD(T) density, we again use the same procedure, but now use the CCSD(T) density and orbitals from a CCSD(T) Lieb maximization at  $\lambda = 0$ , throughout.

In addition to DFA barriers, we also calculate Kohn–Sham barriers purely from CCSD(T) data, which we shall use as reference barriers throughout this work. To do this, we again calculate the  $T_{\text{s}}$ ,  $E_{\text{ext}}$ , and  $E_{\text{J}}$  terms in eqs 28 and 29 directly from the CCSD(T) density and orbitals from a CCSD(T) Lieb maximization at  $\lambda = 0$ . However, for  $\mathcal{W}_{\text{xc},\lambda}[\rho]$ , we use the reference CCSD(T) values of Section 2.4, numerically integrating them as above. Physical barriers determined in this manner agree with standard CCSD(T) barriers—that is, those obtained without any consideration of DFT—to within 0.2 kcal mol<sup>-1</sup>.

It is worth noting that the values of  $C_{\text{R}}$  and the  $E_{\text{J}}$  contribution to  $\mathcal{R}_{\text{Jxc},\lambda}$  are identical for DFA calculations for CCSD(T) densities and for the reference CCSD(T) calculations. This will be pertinent in Sections 3 and 4.

**2.7. Functional-Driven and Density-Driven Errors.** The flexibility to evaluate  $\mathcal{W}_{\text{xc},\lambda}[\rho]$  and Kohn–Sham energy components for various densities (including high-accuracy reference densities) allows for quantification of two distinct sources of error: those arising from errors in the density and those arising from errors in the DFA. Following Kim et al.,<sup>39</sup> we write the error in a given quantity,  $Q$ , obtained from a self-consistent calculation using a DFA, as

$$\Delta Q = Q_{\text{DFA}}[\rho_{\text{DFA}}] - Q_{\text{exact}}[\rho_{\text{exact}}] = \Delta Q_{\text{D}} + \Delta Q_{\text{F}} \quad (30)$$

where the *density-driven* error,

$$\Delta Q_D = Q_{\text{DFA}}[\rho_{\text{DFA}}] - Q_{\text{DFA}}[\rho_{\text{exact}}] \quad (31)$$

arises from the error in the density when a DFA is used, while the *functional-driven* error,

$$\Delta Q_F = Q_{\text{DFA}}[\rho_{\text{exact}}] - Q_{\text{exact}}[\rho_{\text{exact}}] \quad (32)$$

arises from the error in the DFA when the exact density is used. In the context of barriers, we note that  $C_R$  in eq 28 can only have density-driven errors, whereas  $\mathcal{R}_{\text{JC},\lambda}$  in eq 29 may carry functional-driven, as well as density-driven errors.

The main focus of this work will be on functional-driven errors, although we shall consider density-driven errors in Section 4.2. We use the reference CCSD(T) densities as a sufficiently accurate proxy for  $\rho_{\text{exact}}$  in eqs 31 and 32.

### 3. REACTION ADIABATIC-CONNECTION INTEGRAND

To illustrate the adiabatic connection in the context of a chemical reaction, Figure 1 presents the reference CCSD(T) integrand  $\mathcal{W}_{\text{xc},\lambda}[\rho]$ , as a function of  $\lambda$ , for the reactants and transition state in the exchange reaction of H with  $\text{H}_2$  to form  $\text{H}_2$  and H. These are compared with the corresponding (a) LDA,<sup>64,65</sup> (b) PBE,<sup>66</sup> and (c)  $r^2\text{SCAN}$ <sup>67</sup> integrands, determined by evaluating eq 25 for CCSD(T) densities. The difference between the DFA and reference CCSD(T) curves therefore quantifies the functional-driven error, eq 32, in  $\mathcal{W}_{\text{xc},\lambda}[\rho]$ . These DFAs were chosen as representative of the first, second, and third rungs, respectively, of Jacob's Ladder of DFAs.<sup>68</sup> The  $r^2\text{SCAN}$  functional was selected as the representative meta-GGA because it satisfies a wide range of exact constraints while overcoming numerical instabilities associated with the original SCAN functional.<sup>69</sup> (We have also reproduced all calculations in this paper with the TPSS meta-GGA functional<sup>70</sup> and the results are very similar to those of  $r^2\text{SCAN}$ .) We employ reference geometries from the BH76 set in the GMTKN55 database.<sup>71–74</sup>

The reference CCSD(T) curve for the H atom is horizontal, reflecting the fact that there is no electron correlation in a one-electron system and so  $\mathcal{W}_{\text{xc},\lambda}[\rho] = E_{\text{x}}[\rho]$ , see eq 25. By contrast, the reference curves for  $\text{H}_2$  and  $\text{H}_3$  are not horizontal, reflecting the presence of correlation in these systems. However, neither curve exhibits a significant curvature, indicating primarily dynamic correlation, consistent with low-order dependence on the interaction strength, which can be well described by low-order Görling–Levy perturbation theory from their non-interacting Kohn–Sham systems.<sup>32,43,44</sup>

The LDA curves in Figure 1a are in relatively poor agreement with the reference CCSD(T) ones, with all three exhibiting excessive curvature at low  $\lambda$ . For the H atom, the deviation from horizontal reflects a spurious self-interaction in the LDA correlation functional. The PBE curves in Figure 1b are a notable improvement over LDA, although the curve for the H atom is still not quite horizontal, again reflecting spurious self-correlation. By contrast, the  $r^2\text{SCAN}$  curve for the H atom in Figure 1c is horizontal and equal to the reference curve, while the curves for  $\text{H}_2$  and  $\text{H}_3$  resemble those of the PBE functional. The PBE curve is closest to the reference curve for  $\text{H}_3$ , whereas  $r^2\text{SCAN}$  is closest for  $\text{H}_2$ .

In order to quantify the functional-driven errors in the associated barriers, we must compare the DFA barriers determined for CCSD(T) densities with the reference CCSD(T) barriers. From Section 2.6, these DFA and reference barriers both involve the same  $C_R$  in eq 28 and the same  $E_j$  contribution to  $\mathcal{R}_{\text{JC},\lambda}$  in eq 29. Given that the only other contribution to the

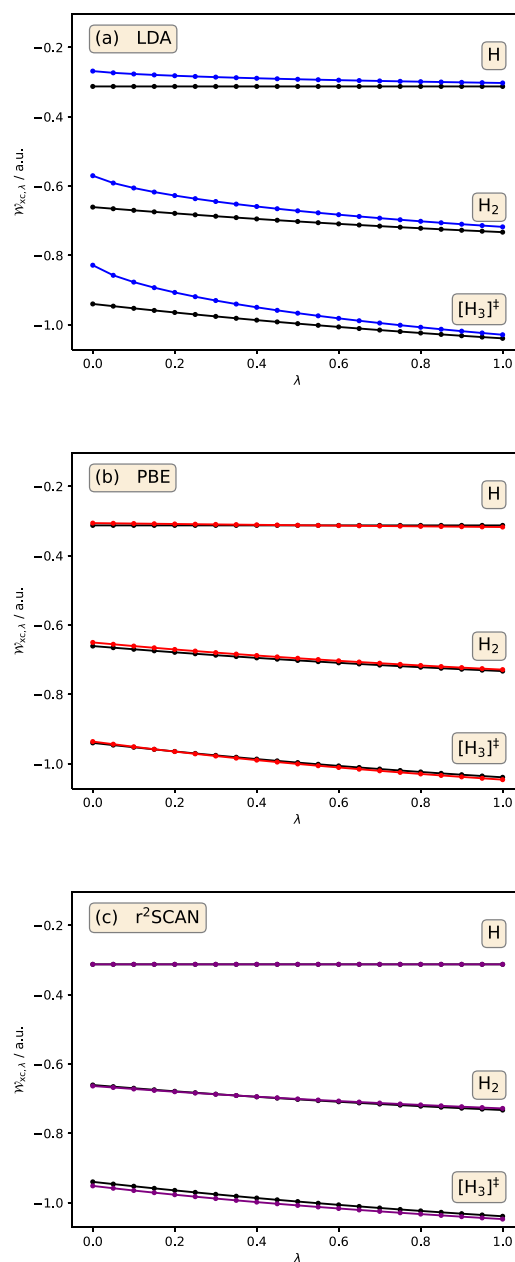


**Figure 1.**  $\mathcal{W}_{\text{xc},\lambda}[\rho]$  for reactants and transition state of the reaction  $\text{H} + \text{H}_2 \rightarrow \text{H}_2 + \text{H}$ , as a function of interaction strength  $\lambda$ , for reference CCSD(T) (black) and (a) LDA (blue), (b) PBE (red), (c)  $r^2\text{SCAN}$  (purple). All DFA  $\mathcal{W}_{\text{xc},\lambda}[\rho]$  are calculated for CCSD(T) densities.

barrier in eq 27 arises from  $\mathcal{W}_{\text{xc},\lambda}[\rho]$  in eq 29, it follows that the differences between the DFA and reference barriers arise entirely due to the differences between the black and colored curves in Figure 1.

Given the relatively subtle differences between the curves in Figure 1, we might hope to obtain relatively accurate DFA barriers—in particular, for PBE and  $r^2\text{SCAN}$ . However, when eq 27 is evaluated for the physical system ( $\lambda = 1$ ), barriers of  $-3.0$ ,  $3.5$ ,  $2.5$ , and  $10.0$  kcal mol<sup>-1</sup> are obtained for LDA, PBE,  $r^2\text{SCAN}$ , and CCSD(T), respectively. The DFA barriers are therefore in very poor agreement with the reference CCSD(T) barrier.

This simple example illustrates that analysis of the individual  $\mathcal{W}_{\text{xc},\lambda}[\rho]$  plots provides limited insight into the associated

barriers. This is, of course, unsurprising given that the plots relate to relatively large individual exchange–correlation energies via eq 10, whereas the barriers relate to relatively small total-energy differences via eq 1. It is therefore instructive to instead consider the  $\mathcal{R}_{\text{xc},\lambda}$  integrand in eq 29 directly. Given that our interest is in barriers of physical systems ( $\lambda = 1$ ), it is convenient to introduce the function,

$$\mathcal{R}_\lambda = C_R + \mathcal{R}_{\text{xc},\lambda} \quad (33)$$

for which

$$\Delta\mathcal{E}_1 = \int_0^1 \mathcal{R}_\lambda d\lambda \quad (34)$$

meaning the “area” between the  $\mathcal{R}_\lambda$  curve and the horizontal axis ( $\mathcal{R}_\lambda = 0$ ), between  $\lambda = 0$  and  $\lambda = 1$ , equals the barrier of the physical system, eq 27 at  $\lambda = 1$ . Note that replacing the upper integral limit in eq 34 by an arbitrary  $\lambda \neq 1$  would not yield  $\Delta\mathcal{E}_\lambda$  because  $C_R$  would be incorrectly scaled by  $\lambda$ . We denote  $\mathcal{R}_\lambda$  a reaction adiabatic-connection integrand and we investigate its utility in Section 4.

#### 4. $\mathcal{R}_\lambda$ FOR REPRESENTATIVE REACTIONS

The hydrogen transfer reaction set, HTBH38,<sup>71</sup> and non-hydrogen transfer reaction set, NHTBH38,<sup>72</sup> of Truhlar and co-workers have been extensively used to evaluate the performance of DFAs, often combined in the BH76 set in the GMTKN55 database.<sup>71–74</sup> We consider a subset of five of these reactions, listed in Table 1, performing all calculations at the database

**Table 1. Benchmark W2-F12<sup>74,75</sup> and CCSD(T) Forward and Reverse Barriers<sup>a</sup>**

reaction	W2-F12		CCSD(T)	
	forward	reverse	forward	reverse
$\text{H} + \text{H}_2 \rightarrow \text{H}_2 + \text{H}$	9.7	9.7	10.0	10.0
$\text{H} + \text{N}_2 \rightleftharpoons \text{HN}_2$	14.6	10.9	15.6	10.2
$\text{HCN} \rightleftharpoons \text{CNH}$	48.1	33.0	48.0	33.0
$\text{H}_2 + \text{OH} \rightleftharpoons \text{H}_2\text{O} + \text{H}$	5.2	21.6	6.6	20.6
$\text{H}_2 + \text{CH}_3 \rightleftharpoons \text{H} + \text{CH}_4$	11.9	15.0	12.2	15.3

<sup>a</sup>All values in kcal mol<sup>-1</sup>.

reference geometries. For each reaction, the table presents high-accuracy benchmark barriers at the W2-F12 level of theory for the GMTKN55 database.<sup>74,75</sup> Also shown are standard CCSD(T) barriers. In all cases, the CCSD(T) barriers agree with the benchmark W2-F12 barriers to better than 1.5 kcal mol<sup>-1</sup>, confirming that the CCSD(T)/cc-pCVTZ level of theory is of sufficient accuracy. Preliminary calculations highlighted the need for triple excitations to achieve this level of agreement. A detailed discussion of basis-set convergence of the reaction barriers at the coupled-cluster level can be found in the Supporting Information.

**4.1. Functional-Driven Errors in  $\mathcal{R}_\lambda$  and Barriers.** We commence by comparing plots of reference CCSD(T)  $\mathcal{R}_\lambda$ , eq 33, as a function of  $\lambda$ , and their associated barriers, eq 34, with those determined from DFAs for CCSD(T) densities. All terms are calculated as described in Section 2.6. Differences again quantify functional-driven errors. Studies<sup>76–78</sup> indicate that functional-driven errors in barriers are typically negative and of significant magnitude for semilocal DFAs.

**4.1.1.  $\text{H} + \text{H}_2 \rightarrow \text{H}_2 + \text{H}$ .** First, we revisit the exchange reaction considered in Section 3. Figure 2 presents the reference CCSD(T)  $\mathcal{R}_\lambda$ , compared to approximate  $\mathcal{R}_\lambda$  for LDA, PBE, and r<sup>2</sup>SCAN. Note that the vertical scale is now in kcal mol<sup>-1</sup>.

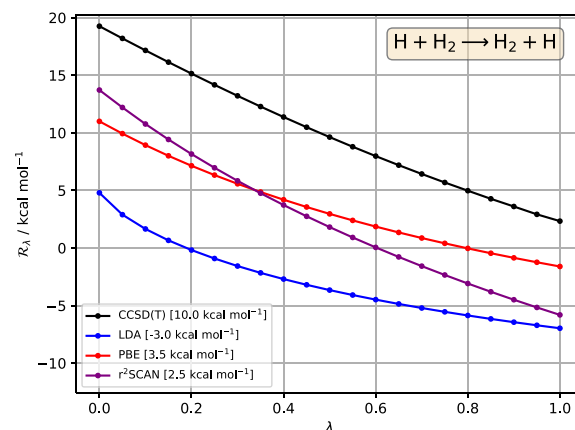


**Figure 2.**  $\mathcal{R}_\lambda$  in eq 33, for the reaction  $\text{H} + \text{H}_2 \rightarrow \text{H}_2 + \text{H}$ , as a function of interaction strength  $\lambda$ , for reference CCSD(T) (black), LDA (blue), PBE (red), r<sup>2</sup>SCAN (purple). All DFA  $\mathcal{R}_\lambda$  are calculated for CCSD(T) densities. The barrier for each method—given in the legend—is the area between the  $\mathcal{R}_\lambda$  curve and the horizontal axis ( $\mathcal{R}_\lambda = 0$ ).

The area between the reference CCSD(T) curve and the horizontal axis is the aforementioned reference barrier of 10.0 kcal mol<sup>-1</sup>. The LDA curve is significantly below the reference curve and the negative area/barrier (−3.0 kcal mol<sup>-1</sup>) is clearly evident. The PBE and r<sup>2</sup>SCAN curves more closely resemble the reference curve, with correspondingly larger areas/barriers, although errors remain significant; it is clear from the areas that the PBE barrier (3.5 kcal mol<sup>-1</sup>) is slightly larger and more accurate than that of r<sup>2</sup>SCAN (2.5 kcal mol<sup>-1</sup>), although both still strongly underestimate the reference value. Figure 2 clearly illustrates negative functional-driven errors, consistent with refs 76–78.

As well as providing a simple way to “visualize” the barrier, a key feature of  $\mathcal{R}_\lambda$  computed in this manner is that it allows a clean separation of the role of exchange and correlation contributions to the barrier, due to the scaling property in eq 25. From eqs 25, 28, 29, and 33, together with the fact that all methods yield the same value of  $C_R$  and the same  $E_J$  contribution to  $\mathcal{R}_{\text{xc},\lambda}$ , the accuracy of  $\mathcal{R}_0$  (i.e., the left-hand points in Figure 2) is determined entirely by the accuracy of the exchange DFA. The value of  $\mathcal{R}_0$  in Figure 2 is strongly underestimated for LDA, somewhat improved for PBE and improved further for r<sup>2</sup>SCAN, although the discrepancy remains significant. By contrast, the shape of  $\mathcal{R}_\lambda$  is determined entirely by the correlation DFA. It is clear from Figure 2 that the behavior of LDA correlation under the scaling relation of eq 25 is poor, reflected by relatively strong curvature in  $\mathcal{R}_\lambda$  compared with the CCSD(T) reference curve. For PBE correlation,  $\mathcal{R}_\lambda$  is less curved but is still far from parallel to the reference curve. For r<sup>2</sup>SCAN correlation,  $\mathcal{R}_\lambda$  becomes most parallel to the reference curve.

Interestingly, despite the aforementioned improvements in both  $\mathcal{R}_0$  and the shape of  $\mathcal{R}_\lambda$  from PBE to r<sup>2</sup>SCAN, the barrier (area) actually degrades because the increase in barrier associated with the improved exchange (improved  $\mathcal{R}_0$ ) is more than compensated by the decrease in barrier associated

with the improved correlation (improved shape of  $\mathcal{R}_\lambda$ ). Put another way, PBE benefits from error cancellation between exchange and correlation, whereas  $r^2$ SCAN does not.

It is well-known that introducing an amount of exact (orbital) exchange into an approximate functional, to yield a hybrid functional, often increases the value of, and hence improves the accuracy of barriers. The aforementioned separation of the role of exchange and correlation contributions in  $\mathcal{R}_\lambda$  makes the introduction of exact exchange particularly simple to visualize: as the amount of exact exchange increases from 0 to 100%, the shape of  $\mathcal{R}_\lambda$  is unchanged, but the curve shifts vertically, such that  $\mathcal{R}_0$  shifts from that of the 0% functional to that of the reference CCSD(T) curve. This is illustrated in Figure 3, which

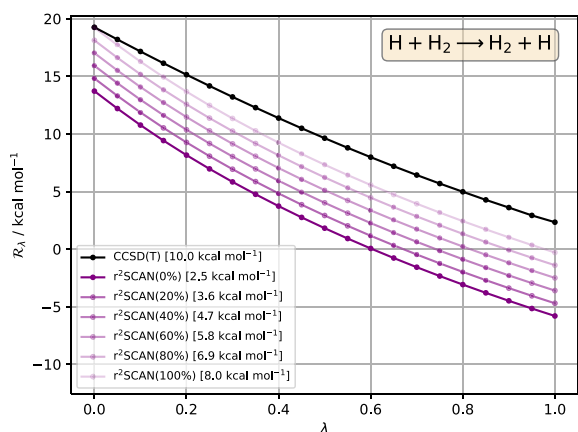


**Figure 3.**  $\mathcal{R}_\lambda$  in eq 33, for the reaction  $\text{H} + \text{H}_2 \rightarrow \text{H}_2 + \text{H}$ , as a function of interaction strength  $\lambda$ , for reference CCSD(T) (black) and  $r^2$ SCAN hybrid functionals, with varying amounts of exact (orbital) exchange indicated in parentheses (purple lines, lighter shading indicates more exact exchange). The pure  $r^2$ SCAN functional is written as  $r^2$ SCAN(0%). All DFA  $\mathcal{R}_\lambda$  are calculated for CCSD(T) densities. The barrier for each method—given in the legend—is the area between the  $\mathcal{R}_\lambda$  curve and the horizontal axis ( $\mathcal{R}_\lambda = 0$ ).

plots  $\mathcal{R}_\lambda$  for hybrid versions of the  $r^2$ SCAN functional, from 0% (conventional  $r^2$ SCAN) to 100%. The optimal barrier (area) of 8 kcal mol<sup>-1</sup> is obtained with 100% exchange. (We only consider

amounts in the range 0% – 100% in this work). To address the remaining 2 kcal mol<sup>-1</sup> error in a rigorous manner, it is necessary to consider improvements to the correlation DFA in order to fix the shape of  $\mathcal{R}_\lambda$ . Access to accurate  $\mathcal{R}_\lambda$  may therefore be desirable for functional development and testing.

The reaction of H with  $\text{H}_2$  is a simple case, which is symmetric in the forward and reverse directions. We now consider other representative reactions from the BH76 set to illustrate the utility of  $\mathcal{R}_\lambda$  more broadly.

**4.1.2.  $\text{H} + \text{N}_2 \rightleftharpoons \text{HN}_2$ .** As an example of an asymmetric reaction from the BH76 set, where the forward and reverse directions are different, we consider the addition reaction of H with  $\text{N}_2$  to form  $\text{HN}_2$  and the reverse dissociation process. Figure 4a,b present the reference CCSD(T)  $\mathcal{R}_\lambda$  for the forward and reverse reactions, respectively, compared to approximate  $\mathcal{R}_\lambda$  for LDA, PBE, and  $r^2$ SCAN.

First, consider the forward reaction  $\text{H} + \text{N}_2 \rightarrow \text{HN}_2$  in Figure 4a. In moving from LDA to PBE to  $r^2$ SCAN, the behavior closely resembles what was observed for  $\text{H} + \text{H}_2 \rightarrow \text{H}_2 + \text{H}$ , with an improvement in  $\mathcal{R}_0$  and the shape of the  $\mathcal{R}_\lambda$  curve from LDA to PBE to  $r^2$ SCAN, but a slight degradation in the barrier from PBE to  $r^2$ SCAN.

By contrast, for the reverse reaction  $\text{HN}_2 \rightarrow \text{H} + \text{N}_2$  in Figure 4b, all three DFAs yield rather similar  $\mathcal{R}_\lambda$  curves, none of which bear much resemblance to the reference CCSD(T) curve. The areas between these curves and the horizontal axis are, however, reasonably close to that of the reference curve due to error cancellation between low- and high- $\lambda$  regions. Hence the barriers are reasonably good—LDA is actually best—with a maximum error of 0.7 kcal mol<sup>-1</sup>. But each gives approximately the right answer for the wrong reason. It is interesting that, for this reverse reaction, the reference  $\mathcal{R}_\lambda$  exhibits strong curvature in the low- $\lambda$  region, which is not captured by any of the DFAs. In fact, the DFAs have a qualitatively different shape, suggesting that the  $\lambda$ -dependence of the correlation contributions according to eq 25 could be significantly improved in the reverse dissociation reaction.

Figure 5a,b present the effect of exact exchange for hybrid versions of  $r^2$ SCAN, for the forward and reverse reactions, respectively. For the forward reaction, the barrier improves steadily as the amount of exchange increases, with an optimal

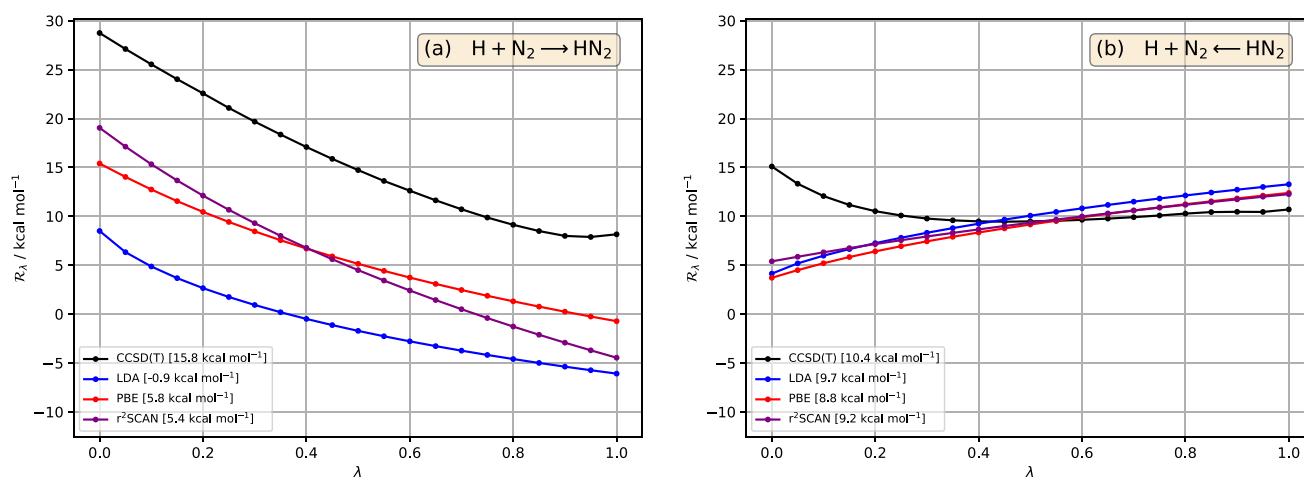


**Figure 4.**  $\mathcal{R}_\lambda$  in eq 33, for the reaction  $\text{H} + \text{N}_2 \rightleftharpoons \text{HN}_2$ , as a function of interaction strength  $\lambda$ , in (a) forward and (b) reverse directions, for reference CCSD(T) (black), LDA (blue), PBE (red),  $r^2$ SCAN (purple). All DFA  $\mathcal{R}_\lambda$  are calculated for CCSD(T) densities. The barrier for each method—given in the legend—is the area between the  $\mathcal{R}_\lambda$  curve and the horizontal axis ( $\mathcal{R}_\lambda = 0$ ).

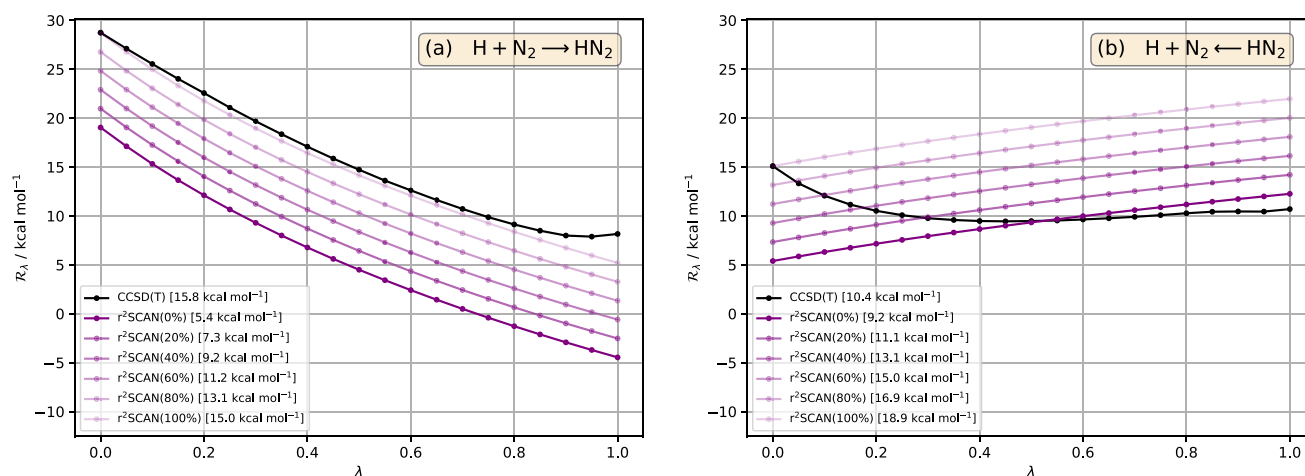


**Figure 5.**  $\mathcal{R}_\lambda$  in eq 33, for the reaction  $\text{H} + \text{N}_2 \rightleftharpoons \text{HN}_2$ , as a function of interaction strength  $\lambda$ , in (a) forward and (b) reverse directions, for reference CCSD(T) (black) and  $r^2\text{SCAN}$  hybrid functionals, with varying amounts of exact (orbital) exchange indicated in parentheses (purple lines, lighter shading indicates more exact exchange). The pure  $r^2\text{SCAN}$  functional is written as  $r^2\text{SCAN}(0\%)$ . All DFA  $\mathcal{R}_\lambda$  are calculated for CCSD(T) densities. The barrier for each method—given in the legend—is the area between the  $\mathcal{R}_\lambda$  curve and the horizontal axis ( $\mathcal{R}_\lambda = 0$ ).

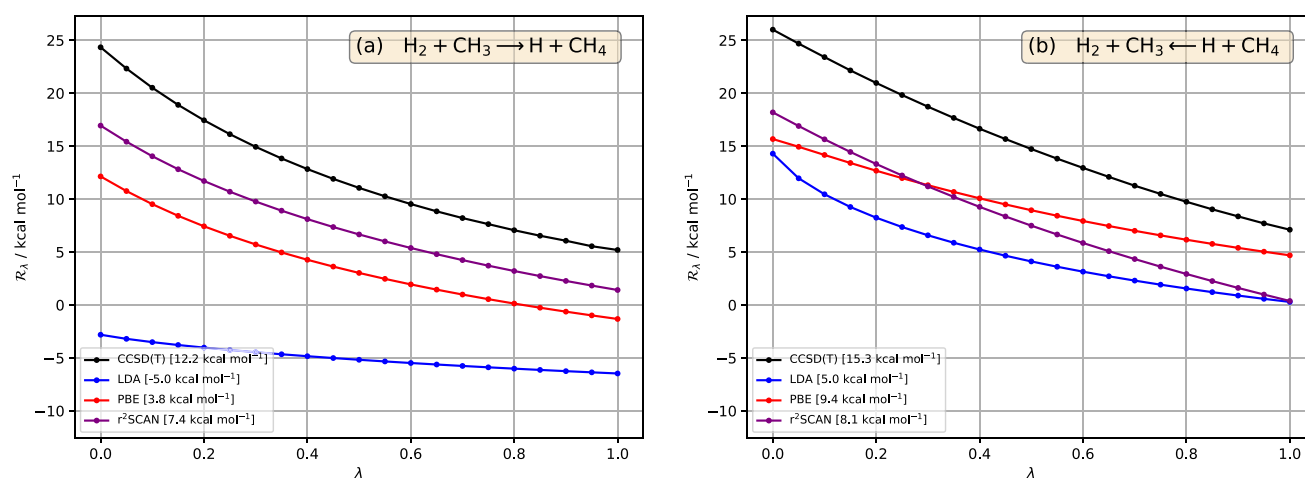


**Figure 6.**  $\mathcal{R}_\lambda$  in eq 33, for the reaction  $\text{H}_2 + \text{CH}_3 \rightleftharpoons \text{H} + \text{CH}_4$ , as a function of interaction strength  $\lambda$ , in (a) forward and (b) reverse directions, for reference CCSD(T) (black), LDA (blue), PBE (red),  $r^2\text{SCAN}$  (purple). All DFA  $\mathcal{R}_\lambda$  are calculated for CCSD(T) densities. The barrier for each method—given in the legend—is the area between the  $\mathcal{R}_\lambda$  curve and the horizontal axis ( $\mathcal{R}_\lambda = 0$ ).

value at 100%, giving an error of just 0.8 kcal mol<sup>-1</sup>. By contrast, for the reverse reaction, an amount between 0 and 20% is optimal; using 100% dramatically overestimates the barrier.

Once again, this difference highlights the key interplay between exchange and correlation. If the correlation functional is accurate (in the sense that the correlation part of eq 25 resembles that of the reference CCSD(T) curve), then the shape of  $\mathcal{R}_\lambda$  will be similar to that of the reference curve and so  $\sim 100\%$  exchange will be optimal for the barrier, since only then can the areas from the DFA and reference curves be approximately the same. However, if the correlation functional is poor, then the shape of  $\mathcal{R}_\lambda$  will be very different to that of the reference curve and so the optimal amount of exchange must differ from 100%; an accurate barrier will then be a consequence of error cancellation between different  $\lambda$  regions. In terms of the functional components, the residual exchange in the latter case compensates for the error in the correlation functional.

**4.1.3. HCN  $\rightleftharpoons$  CNH and  $\text{H}_2 + \text{OH} \rightleftharpoons \text{H}_2\text{O} + \text{H}$ .** Results for the rearrangement of HCN to CNH and the hydrogen abstraction reaction of  $\text{H}_2$  with OH to form  $\text{H}_2\text{O}$  and H, together with their

reverse reactions, are presented in the Supporting Information. As in Section 4.1.2, the key result is that the shape of  $\mathcal{R}_\lambda$  is notably better reproduced by  $r^2\text{SCAN}$  in one direction than the other, with the consequence that the optimal amount of exchange is much higher in one direction than the other.

**4.1.4.  $\text{H}_2 + \text{CH}_3 \rightleftharpoons \text{H} + \text{CH}_4$ .** As a final representative reaction from the BH76 set, we consider the hydrogen abstraction reaction of  $\text{H}_2$  with  $\text{CH}_3$  to form H and  $\text{CH}_4$ , and the reverse reaction; see Figures 6 and 7. For the forward reaction in Figure 6a, there is marked improvement in the  $\mathcal{R}_\lambda$  curve and the barrier from LDA to PBE to  $r^2\text{SCAN}$ . The LDA functional exhibits too little curvature and a negative barrier. The  $\mathcal{R}_\lambda$  curves for PBE and  $r^2\text{SCAN}$  now exhibit a similar shape and so the improvement in  $\mathcal{R}_0$  from PBE to  $r^2\text{SCAN}$  leads to an improved barrier. For the reverse reaction in Figure 6b, the situation resembles that in Section 4.1.1 and the forward reaction in Section 4.1.2.

Of all the nonsymmetric reactions considered, this is the one where the quality of the shape of  $\mathcal{R}_\lambda$  from  $r^2\text{SCAN}$  is most similar between the forward and reverse reactions. It follows that both directions benefit from reasonably large amounts of exact

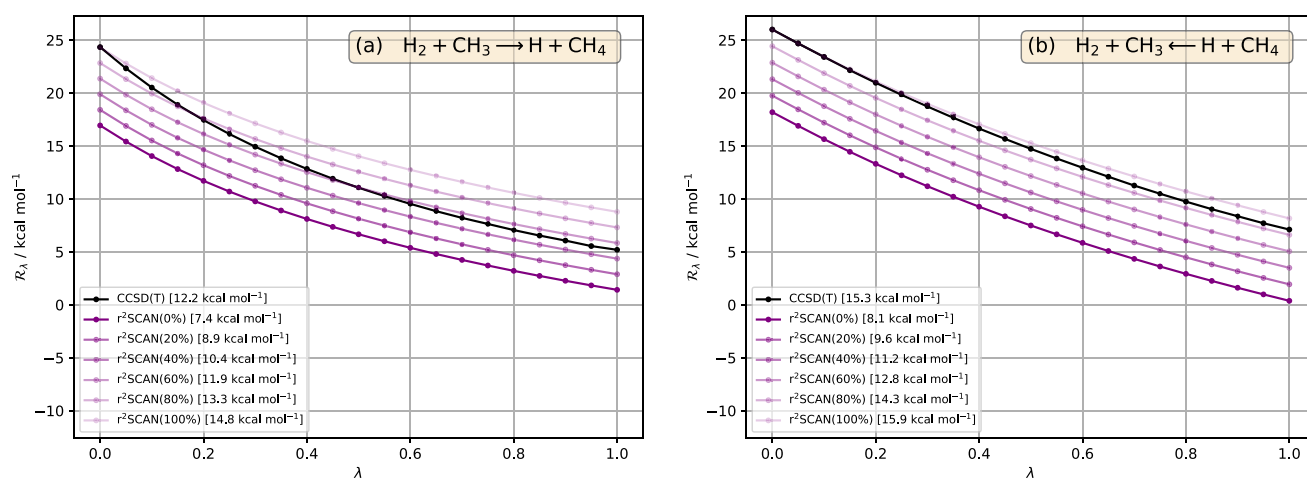


**Figure 7.**  $\mathcal{R}_\lambda$  in eq 33, for the reaction  $\text{H}_2 + \text{CH}_3 \rightleftharpoons \text{H} + \text{CH}_4$ , as a function of interaction strength  $\lambda$ , in (a) forward and (b) reverse directions, for reference CCSD(T) (black) and  $r^2\text{SCAN}$  hybrid functionals, with varying amounts of exact (orbital) exchange indicated in parentheses (purple lines, lighter shading indicates more exact exchange). The pure  $r^2\text{SCAN}$  functional is written as  $r^2\text{SCAN}(0\%)$ . All DFA  $\mathcal{R}_\lambda$  are calculated for CCSD(T) densities. The barrier for each method—given in the legend—is the area between the  $\mathcal{R}_\lambda$  curve and the horizontal axis ( $\mathcal{R}_\lambda = 0$ ).

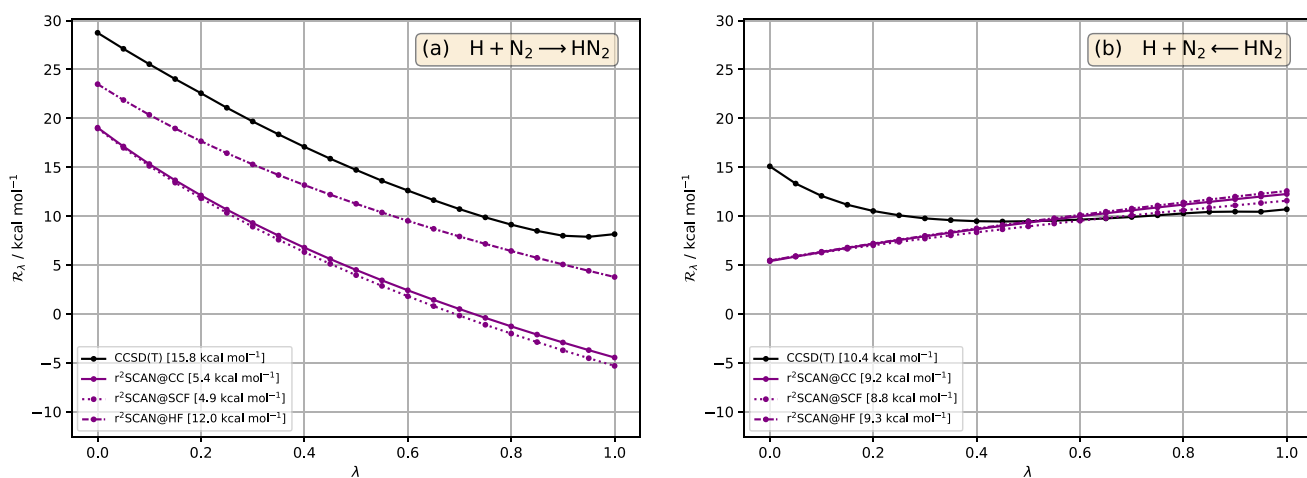


**Figure 8.**  $\mathcal{R}_\lambda$  in eq 33, for the reaction  $\text{H} + \text{N}_2 \rightleftharpoons \text{HN}_2$ , as a function of interaction strength  $\lambda$ , in (a) forward and (b) reverse directions, for reference CCSD(T) (black),  $r^2\text{SCAN}@SCF$  (purple, dotted),  $r^2\text{SCAN}@HF$  (purple, dot-dashed),  $r^2\text{SCAN}@CC$  (purple). The barrier for each method—given in the legend—is the area between the  $\mathcal{R}_\lambda$  curve and the horizontal axis ( $\mathcal{R}_\lambda = 0$ ).

exchange, as illustrated in Figure 7. The optimal amount for the forward reaction, just above 60%, is less than for the reverse reaction, which is 80–100%, reflecting the fact that the  $r^2\text{SCAN}$  DFA curves are slightly more parallel to the reference CCSD(T) curve for the reverse reaction than for the forward reaction.

**4.2. Density-Driven Errors in  $\mathcal{R}_\lambda$  and Barriers.** Kaplan et al.,<sup>76</sup> Kanungo et al.,<sup>77</sup> and Hernandez et al.<sup>78</sup> recently investigated the role of functional-driven and density-driven errors in barrier calculations. Their key observation was that the density-driven errors in eq 31 are generally much smaller than the functional-driven errors in eq 32, meaning the overall error in eq 30 is generally dominated by the functional-driven error. However, when they replaced the self-consistent DFA density in these equations with the Hartree–Fock density, the analogue of the density-driven error in eq 31 could become large and positive, leading to some degree of error cancellation with the (unchanged) functional-driven error, meaning the overall error in the barrier could become much smaller.

Here, we investigate this observation from the perspective of  $\mathcal{R}_\lambda$  by comparing  $r^2\text{SCAN}$   $\mathcal{R}_\lambda$  curves for self-consistent densities, Hartree–Fock densities, and CCSD(T) densities.

**4.2.1.  $\text{H} + \text{N}_2 \rightleftharpoons \text{HN}_2$ .** Figure 8 presents the reaction adiabatic-connection integrand  $\mathcal{R}_\lambda$  of the forward and reverse  $\text{H} + \text{N}_2 \rightleftharpoons \text{HN}_2$  reactions for the  $r^2\text{SCAN}$  functional, evaluated for three different densities: the self-consistent density ( $r^2\text{SCAN}@SCF$ ), the Hartree–Fock density ( $r^2\text{SCAN}@HF$ ), and the CCSD(T) density ( $r^2\text{SCAN}@CC$ ). We have also included the reference CCSD(T) curve. The CCSD(T) and  $r^2\text{SCAN}@CC$  curves have previously been presented in Figure 4, in our discussion of functional-driven errors; in that plot, the  $r^2\text{SCAN}@CC$  curve was denoted  $r^2\text{SCAN}$ .

For the forward reaction in Figure 8a, the  $r^2\text{SCAN}@SCF$  curve is close to the  $r^2\text{SCAN}@CC$  curve, indicating that the density-driven error in  $\mathcal{R}_\lambda$  is small and that, on average, the  $r^2\text{SCAN}$  densities/orbitals are reasonably close to those from CCSD(T). By contrast, the  $r^2\text{SCAN}@HF$  curve is notably above the  $r^2\text{SCAN}@CC$  curve and closer to the reference CCSD(T) curve, indicating that the Hartree–Fock analogue of the density-

driven error is large and positive and goes some way toward canceling the functional-driven error. It is important to note, however, that this improvement is obtained at the expense of a degraded density. For the reverse reaction in Figure 8b, the effect is much less pronounced, with the  $r^2\text{SCAN}@CC$ ,  $r^2\text{SCAN}@SCF$ , and  $r^2\text{SCAN}@HF$  curves close together, indicating that the functional-driven error dominates, irrespective of the density used.

The shapes of the three  $r^2\text{SCAN}$  curves for the forward reaction in Figure 8a are rather similar, indicating that the correlation scaling property in eq 25 is relatively insensitive to variations in the density. The same is observed for the reverse reaction in Figure 8b. The reason why the Hartree–Fock density has such a pronounced effect for the forward reaction, but not the reverse reaction, is therefore largely because the value of  $\mathcal{R}_0$  changes significantly from  $r^2\text{SCAN}@SCF$  to  $r^2\text{SCAN}@HF$  in the former, but not the latter. For these calculations, differences in  $\mathcal{R}_0$  between  $r^2\text{SCAN}@SCF$  and  $r^2\text{SCAN}@HF$  arise not only from the use of different densities in the exchange terms in  $\mathcal{R}_{jxc,\lambda}$  in eq 29, but also from different values of  $C_R$  in eq 28 and  $E_j$  terms in  $\mathcal{R}_{jxc,\lambda}$ . This contrasts the functional-driven analysis in Section 4.1, where the use of the CCSD(T) density throughout led to the same  $C_R$  and  $E_j$  terms.

An analysis of how the aforementioned terms change from  $r^2\text{SCAN}@SCF$  to  $r^2\text{SCAN}@HF$ , for both the forward and reverse reaction, offers little insight into the different behavior of  $\mathcal{R}_0$ . All terms make non-negligible contributions to the change in  $\mathcal{R}_0$ , the largest magnitudes being the  $T_s$  and  $E_{\text{ext}}$  components of  $C_R$  for the forward and reverse reactions, respectively.

**4.2.2. Other Reactions.** Results for the hydrogen exchange reaction  $\text{H} + \text{H}_2 \rightarrow \text{H}_2 + \text{H}$ , for the rearrangement  $\text{HCN} \rightleftharpoons \text{CNH}$ , and for the hydrogen abstraction reactions  $\text{H}_2 + \text{OH} \rightleftharpoons \text{H}_2\text{O} + \text{H}$  and  $\text{H}_2 + \text{CH}_3 \rightleftharpoons \text{H} + \text{CH}_4$  are presented in the Supporting Information and they show a similar picture: In all cases, the density-driven error in  $\mathcal{R}_\lambda$  is small. When the self-consistent density is replaced with the Hartree–Fock density, the effect can be pronounced, leading to some degree of cancellation with the functional-driven error. An analysis of the components of  $\mathcal{R}_0$  again offers little insight into the different behaviors.

The  $\mathcal{R}_\lambda$  observations in Sections 4.2.1 and 4.2.2 translate into barrier observations, through eq 34, that are fully consistent with those of refs 76–78 while providing additional insight into those observations.

**4.2.3. Density-Corrected DFT.** The idea of using Hartree–Fock quantities in DFAs to improve barriers is not new. It was proposed in the so-called HF-DFT<sup>79–81</sup> and a similar idea has recently gained popularity as density-corrected DFT (DC-DFT).<sup>39,82–87</sup> The application of DC-DFT is somewhat more nuanced, in that the density-sensitivity of a molecule,<sup>84</sup>

$$\tilde{S} = |\tilde{E}[\rho_{\text{LDA}}] - \tilde{E}[\rho_{\text{HF}}]| \quad (35)$$

is quantified by evaluating the absolute change in the total energy for the chosen DFA, when using the LDA density  $\rho_{\text{LDA}}$  and the Hartree–Fock density  $\rho_{\text{HF}}$ . Since LDA tends to significantly overdelocalize densities, while Hartree–Fock tends to significantly overlocalize densities, this difference gives an indication of the sensitivity of the selected DFA to changes in the density. It has been suggested<sup>84</sup> that, when  $\tilde{S} > 2$  kcal mol<sup>-1</sup> for small molecules, then the system is density-sensitive and DC-DFT should be applied. For the  $\text{H} + \text{N}_2 \rightleftharpoons$

$\text{HN}_2$  reaction using the  $r^2\text{SCAN}$  functional, this threshold is surpassed for  $\text{N}_2$ ,  $\text{HN}_2$  and the  $[\text{HN}_2]^\ddagger$  transition state, with values of 2.5, 8.4, and 8.7 kcal mol<sup>-1</sup>, respectively. For the H atom, the density sensitivity value is just 0.3 kcal mol<sup>-1</sup>.

The  $r^2\text{SCAN}@HF$  curves in Figure 8 correspond to using the DC-DFT approach for all species, including the H atom. The associated barriers are larger (and more accurate) than the conventional barriers, associated with the  $r^2\text{SCAN}@SCF$  curves. The fact that this is so much more pronounced for the forward reaction is fully consistent with the thresholds: while the  $[\text{HN}_2]^\ddagger$  transition state is density-sensitive with  $\tilde{S} = 8.7$  kcal mol<sup>-1</sup>, the reactants are relatively density-insensitive, with  $\tilde{S} = 0.3$  kcal mol<sup>-1</sup> for H and  $\tilde{S} = 2.5$  kcal mol<sup>-1</sup> for  $\text{N}_2$ . As a result, the use of the HF density raises the energy of the transition state relative to the (variationally optimal) self-consistent energy by more than it raises the energy of the reactants, resulting in a significant increase in the  $r^2\text{SCAN}@HF$  barrier compared with that of  $r^2\text{SCAN}@SCF$ . For the reverse reaction, the transition state is only marginally more density-sensitive than the reactant, with  $\tilde{S}$  values of 8.7 and 8.4 kcal mol<sup>-1</sup> respectively. As a result the effect of using the HF density is to raise the energy of the reactant and transition state by approximately the same amount, leading to relatively little change in the barrier.

In a recent study, Hernandez et al.<sup>78</sup> also examined the issue of error cancellations when applying DC-DFT to calculate barriers, reaching similar conclusions. As part of their study, the authors also proposed a second criterion to check that the Hartree–Fock density is reasonable for use in DC-DFT. Specifically, the degree of spin-contamination  $|\langle S^2 \rangle_{\text{HF}} - \langle S^2 \rangle_{\text{exact}}|$  should not exceed 10% for open-shell systems. For the  $[\text{HN}_2]^\ddagger$  transition state, this value is 20.1%, while for the product  $\text{HN}_2$ , it is 17.1%, suggesting that DC-DFT may not be suitable for use in either the forward or reverse reaction. In the present work, calculations at the  $r^2\text{SCAN}@HF$  level are used merely to quantify the effect of changing the density, which is of interest regardless of whether DC-DFT should be applied practically. Finally, it should also be noted that the criteria for applying DC-DFT are heavily sensitive to the choice of DFA. For the 15 systems comprising the 5 reactions studied in this work, the combined  $\tilde{S}$  and  $\langle S^2 \rangle$  criteria suggest that only 5 systems should be corrected for  $r^2\text{SCAN}$ . This increases to 11 for both the LDA and PBE functionals.

## 5. CONCLUSIONS

The calculation of classical reaction barriers has long been challenging for semilocal DFAs, which have a tendency to severely underestimate these quantities. We have examined these shortcomings from a new perspective—namely, that of the density-fixed adiabatic connection, which links the Kohn–Sham noninteracting system to the physical interacting system. A reaction adiabatic-connection integrand,  $\mathcal{R}_\lambda$ , was introduced, such that integration over the interaction strength,  $\lambda$ , from 0 to 1 yields the barrier, meaning the barrier can be easily visualized as the area under a plot of  $\mathcal{R}_\lambda$  vs  $\lambda$ .

Initially, we focused on functional-driven errors by comparing reference  $\mathcal{R}_\lambda$  curves obtained from CCSD(T) Lieb maximizations with density-functional approximations to these curves for LDA, PBE, and  $r^2\text{SCAN}$ , determined using coordinate scaling for CCSD(T) densities. By fixing the densities to be those obtained from the CCSD(T) wave function, our analysis provides a simple way to visualize and understand functional-driven errors and trends in barriers from approximate functionals, while allowing a clean separation of the role of exchange

and correlation contributions to the barrier. Specifically, the accuracy of  $\mathcal{R}_0$  is determined entirely by the accuracy of the exchange DFA, while the shape of  $\mathcal{R}_\lambda$  is determined entirely by the correlation functional.

As may be expected, the value of  $\mathcal{R}_0$  tended to improve from LDA to PBE to  $r^2$ SCAN. Increasing the fraction of exact (orbital) exchange to form hybrid functionals has a particularly simple effect on the  $\mathcal{R}_\lambda$  curves: it shifts them vertically, improving the value of  $\mathcal{R}_0$ , until the reference CCSD(T) value is recovered with 100% exchange.

Obtaining the correct shape of  $\mathcal{R}_\lambda$  was more challenging. In some reactions, the shape of  $\mathcal{R}_\lambda$  was reasonably well described, in which case increasing the amount of exact exchange to close to 100% led to a significant improvement in the barrier. However, in other cases the shape of  $\mathcal{R}_\lambda$  was poorly described and, while a modest increase in the amount of exact exchange did lead to a nominal improvement in the barrier due to cancellation of errors in high and low  $\lambda$  regions, this is nothing more than error compensation between the exchange and correlation contributions. We note that for the four reactions where the forward and reverse directions are different, the shape of  $\mathcal{R}_\lambda$  is best described for the direction with the larger barrier, i.e. the direction with the later transition state. However, the amount of data is limited and so further investigation is required to establish if this trend is more widely applicable.

These results illustrate how simply introducing larger amounts of exact exchange may not be a reliable approach to generate improved functionals for barriers, especially since the amount required for forward and reverse directions of the same reaction may be significantly different. To make significant progress, the shape of  $\mathcal{R}_\lambda$  must be captured more accurately. Since the shape is determined *entirely* by the correlation functional and its scaling properties according to eq 25, it would be fruitful to consider design of functionals parametrized to more accurately reproduce the shape of  $\mathcal{R}_\lambda$ . The results reported here present a first step toward benchmark numerical data that may be useful for this purpose and this will be pursued in future work.

We then considered density-driven errors, comparing self-consistent  $r^2$ SCAN results for  $\mathcal{R}_\lambda$  with those evaluated using  $r^2$ SCAN for the reference CCSD(T) density. The self-consistent  $\mathcal{R}_\lambda$  curves remained close to those evaluated for the reference CCSD(T) density, indicating that the density-driven error is small and that, at least on average, the  $r^2$ SCAN densities/orbitals of each species involved in the reactions studied are close to the CCSD(T) ones. Using the Hartree–Fock density instead, as is done in HF-DFT and DC-DFT, could lift the  $\mathcal{R}_\lambda$ , bringing it closer to the reference CCSD(T) curve, reflecting some degree of cancellation with the functional-driven errors, consistent with recent studies.<sup>76–78</sup> However, given that the associated improvements in the barriers are not a result of an improved density, barriers obtained using HF-DFT and DC-DFT should be treated with some caution.

Finally, we also considered the use of the density-sensitivity measure  $\bar{S}$  of eq 35 and the spin-contamination criterion of Hernandez et al.<sup>78</sup> Our  $\mathcal{R}_\lambda$  and barrier results for a representative reaction are fully consistent with the values of  $\bar{S}$ , whereby similar sensitivities in the reactant/transition state lead to a small effect on the reverse barrier, whereas very different sensitivities in reactant/transition state led to a much larger effect on the forward barrier.

In this work, we have focused on simple semilocal approximations, since these represent some of the most cost-effective methods in widespread application. However, range-separated hybrids often give rise to much improved barriers when tested on, for example, the BH76 benchmark set. An interesting avenue for future work is therefore to use a generalized adiabatic connection to study such functional forms. Indeed, such calculations can be carried out with the framework used in the present work, as shown in ref 88. Alternative adiabatic connections, where the electron density is not held fixed, could also be considered in a similar manner, for example the potential-fixed adiabatic connection in ref 43., or the Møller–Plesset adiabatic connection in ref 89.; the latter may give additional insight into the performance of approaches that use a Hartree–Fock reference.

We note that errors in barriers are often attributed to self-interaction, which functionals with increased orbital-dependent exchange and approaches such as HF-DFT/DC-DFT are thought to help mitigate. The use of explicit self-interaction corrections has been explored extensively in the recent literature and it would be interesting to analyze how  $\mathcal{R}_\lambda$  is influenced by these approaches.

Finally, our approach for defining an adiabatic-connection integrand for reaction barriers could be applied to many other properties, including the majority of those in the GMTKN55 database. Future work will pursue the construction of adiabatic-connection data sets for a range of quantities, providing extensive data to benchmark new density-functional approximations.

## ■ APPENDIX A

### GDIIS Optimization of $G_{\lambda,p}[\mathbf{b}]$

The GDIIS algorithm<sup>50</sup> is defined by choosing an approximation to the error vectors  $\mathbf{e}_i$  that define the difference between the potential coefficients  $\mathbf{b}_i$  at a particular iteration  $i$  and the converged potential coefficients  $\mathbf{b}^*$ , such that  $\mathbf{b}_i = \mathbf{b}^* + \mathbf{e}_i$ . The error vectors can be approximated by those for a quadratic function,

$$\mathbf{e}_i = -\mathbf{H}^{-1}\mathbf{g}_i \quad (\text{A1})$$

where  $\mathbf{H}$  and  $\mathbf{g}$  are the Hessian and gradient with respect to the coefficients  $\mathbf{b}$ , respectively. A set of potential expansion coefficients and error vectors are generated for  $m$  iterations, defining an  $m$ -dimensional iterative subspace. Minimisation of the residuum vector  $\sum_i c_i \mathbf{e}_i$  subject to the constraint  $\sum_i c_i = 1$  leads to the DIIS equations,

$$\begin{pmatrix} B_{11} & \dots & B_{1m} & 1 \\ \vdots & \ddots & \vdots & \vdots \\ B_{m1} & \dots & B_{mm} & 1 \\ 1 & \dots & 1 & 0 \end{pmatrix} \begin{pmatrix} c_1 \\ \vdots \\ c_m \\ -\zeta \end{pmatrix} = \begin{pmatrix} 0 \\ \vdots \\ 0 \\ 1 \end{pmatrix} \quad (\text{A2})$$

where  $B_{ij} = \langle \mathbf{e}_i | \mathbf{e}_j \rangle$  is the scalar product of the error vectors  $\mathbf{e}_i$  and  $\mathbf{e}_j$  and  $\zeta$  is a Lagrange multiplier. The potential coefficients at the next iteration can then be calculated according to

$$\mathbf{b}_{m+1} = \sum_{i=1}^m c_i \mathbf{b}_i - \mathbf{H}^{-1} \left( \sum_{i=1}^m c_i \mathbf{g}_i \right) \quad (\text{A3})$$

where the coefficients  $c_i$  are determined from A2 and define an interpolated set of coefficients (the first term of A3) and an interpolated gradient (in parentheses in the second term of A3).

The potential coefficients for the next step  $\mathbf{b}_{m+1}$  then correspond to the interpolated coefficients updated by a Newton step constructed using an approximation to the Hessian  $\mathbf{H}$  and the interpolated gradient. In the present work, we use the noninteracting Hessian, given by eq 21 at  $\lambda = 0$ .<sup>49</sup> Since the quadratic approximation of  $\mathbf{A1}$  is only valid close to the maximum of  $G_{\lambda,\rho}[\mathbf{b}]$ , the GDIIS algorithm is switched on when the Euclidean norm of  $\mathbf{g}_i$  falls below  $10^{-4}$  a.u.

## ■ ASSOCIATED CONTENT

### Data Availability Statement

The data that supports the findings of this work are available within the article.

### SI Supporting Information

The Supporting Information is available free of charge at <https://pubs.acs.org/doi/10.1021/acs.jctc.4c01038>.

Details of Lieb maximizations, convergence of reaction barriers with respect to basis set and excitation level in coupled-cluster calculations, and functional-driven and density-driven errors in  $\mathcal{R}_i$  and barriers for additional reactions (PDF)

## ■ AUTHOR INFORMATION

### Corresponding Authors

Andrew M. Wibowo-Teale – School of Chemistry, University of Nottingham, University Park, Nottingham NG7 2RD, U.K.; [orcid.org/0000-0001-9617-1143](https://orcid.org/0000-0001-9617-1143); Email: [andrew.teale@nottingham.ac.uk](mailto:andrew.teale@nottingham.ac.uk)

Trygve Helgaker – Hylleraas Centre for Quantum Molecular Sciences, Department of Chemistry, University of Oslo, N-0315 Oslo, Norway; [orcid.org/0000-0002-5032-8392](https://orcid.org/0000-0002-5032-8392); Email: [trygve.helgaker@kjemi.uio.no](mailto:trygve.helgaker@kjemi.uio.no)

David J. Tozer – Department of Chemistry, Durham University, Durham DH1 3LE, U.K.; [orcid.org/0000-0002-8750-2753](https://orcid.org/0000-0002-8750-2753); Email: [d.j.tozer@durham.ac.uk](mailto:d.j.tozer@durham.ac.uk)

### Author

Bang C. Huynh – School of Chemistry, University of Nottingham, University Park, Nottingham NG7 2RD, U.K.; [orcid.org/0000-0002-5226-4054](https://orcid.org/0000-0002-5226-4054)

Complete contact information is available at: <https://pubs.acs.org/doi/10.1021/acs.jctc.4c01038>

### Notes

The authors declare no competing financial interest.

## ■ ACKNOWLEDGMENTS

We are grateful to Alex Borgoo and Toru Shiozaki for assistance with exploratory adiabatic-connection calculations and useful discussions. This work was supported by the Norwegian Research Council through CoE Hylleraas Centre for Quantum Molecular Sciences Grant No. 262695. A.M.T. is grateful for support from the European Research Council under H2020/ERC Consolidator Grant “topDFT” (Grant No. 772259).

## ■ REFERENCES

- (1) Kohn, W.; Sham, L. J. Self-consistent equations including exchange and correlation effects. *Phys. Rev.* **1965**, *140*, A1133–A1138.
- (2) Burke, K. Perspective on density functional theory. *J. Chem. Phys.* **2012**, *136*, 150901.
- (3) Becke, A. D. Perspective: Fifty years of density-functional theory in chemical physics. *J. Chem. Phys.* **2014**, *140*, 18A301.

- (4) Teale, A. M.; Helgaker, T.; Savin, A.; Adamo, C.; Aradi, B.; Arbuznikov, A. V.; Ayers, P. W.; Baerends, E. J.; Barone, V.; Calamini, P.; Cancès, E.; Carter, E. A.; Chattaraj, P. K.; Chermette, H.; Ciofini, I.; Crawford, T. D.; De Proft, F.; Dobson, J. F.; Draxl, C.; Frauenheim, T.; Fromager, E.; Fuentealba, P.; Gagliardi, L.; Galli, G.; Gao, J.; Geerlings, P.; Gidopoulos, N.; Gill, P. M. W.; Gori-Giorgi, P.; Görling, A.; Gould, T.; Grimme, S.; Gritsenko, O.; Jensen, H. J. A.; Johnson, E. R.; Jones, R. O.; Kaupp, M.; Köster, A. M.; Kronik, L.; Krylov, A. I.; Kvaal, S.; Laestadius, A.; Levy, M.; Lewin, M.; Liu, S.; Loos, P.-F.; Maitra, N. T.; Neese, F.; Perdew, J. P.; Pernal, K.; Pernot, P.; Piecuch, P.; Rebolini, E.; Reining, L.; Romaniello, P.; Ruzsinszky, A.; Salahub, D. R.; Scheffler, M.; Schwerdtfeger, P.; Staroverov, V. N.; Sun, J.; Tellgren, E.; Tozer, D. J.; Trickey, S. B.; Ullrich, C. A.; Vela, A.; Vignale, G.; Wesolowski, T. A.; Xu, X.; Yang, W. DFT exchange: sharing perspectives on the workhorse of quantum chemistry and materials science. *Phys. Chem. Chem. Phys.* **2022**, *24*, 28700–28781.

- (5) Porezag, D.; Pederson, M. R. Density functional based studies of transition states and barriers for hydrogen exchange and abstraction reactions. *J. Chem. Phys.* **1995**, *102*, 9345–9349.

- (6) Zhang, Y.; Yang, W. A challenge for density functionals: Self-interaction error increases for systems with a noninteger number of electrons. *J. Chem. Phys.* **1998**, *109*, 2604–2608.

- (7) Polo, V.; Kraka, E.; Cremer, D. Electron correlation and the self-interaction error of density functional theory. *Mol. Phys.* **2002**, *100*, 1771–1790.

- (8) Dutoi, A. D.; Head-Gordon, M. Self-interaction error of local density functionals for alkali-halide dissociation. *Chem. Phys. Lett.* **2006**, *422*, 230–233.

- (9) Lynch, B. J.; Truhlar, D. G. How well can hybrid density functional methods predict transition state geometries and barrier heights? *J. Phys. Chem. A* **2001**, *105*, 2936–2941.

- (10) Patchkovskii, S.; Ziegler, T. Improving “difficult” reaction barriers with self-interaction corrected density functional theory. *J. Chem. Phys.* **2002**, *116*, 7806–7813.

- (11) Gräfenstein, J.; Kraka, E.; Cremer, D. The impact of the self-interaction error on the density functional theory description of dissociating radical cations: Ionic and covalent dissociation limits. *J. Chem. Phys.* **2004**, *120*, 524–539.

- (12) Lundberg, M.; Siegbahn, P. E. M. Quantifying the effects of the self-interaction error in DFT: When do the delocalized states appear? *J. Chem. Phys.* **2005**, *122*, 224103.

- (13) Zhao, Y.; Truhlar, D. G. Design of density functionals that are broadly accurate for thermochemistry, thermochemical kinetics, and nonbonded interactions. *J. Phys. Chem. A* **2005**, *109*, 5656–5667.

- (14) Xu, X.; Alecu, I. M.; Truhlar, D. G. How well can modern density functionals predict internuclear distances at transition states? *J. Chem. Theory Comput.* **2011**, *7*, 1667–1676.

- (15) Bao, J. L.; Gagliardi, L.; Truhlar, D. G. Self-interaction error in density functional theory: An appraisal. *J. Phys. Chem. Lett.* **2018**, *9*, 2353–2358.

- (16) Mishra, P.; Yamamoto, Y.; Johnson, J. K.; Jackson, K. A.; Zope, R. R.; Baruah, T. Study of self-interaction-errors in barrier heights using locally scaled and Perdew–Zunger self-interaction methods. *J. Chem. Phys.* **2022**, *156*, No. 014306.

- (17) Shukla, P. B.; Mishra, P.; Baruah, T.; Zope, R. R.; Jackson, K. A.; Johnson, J. K. How do self-interaction errors associated with stretched bonds affect barrier height predictions? *J. Phys. Chem. A* **2023**, *127*, 1750–1759.

- (18) Singh, Y.; Peralta, J. E.; Jackson, K. A. The rise and fall of stretched bond errors: Extending the analysis of Perdew–Zunger self-interaction corrections of reaction barrier heights beyond the LSDA. *J. Chem. Phys.* **2024**, *160*, 124105.

- (19) Ruzsinszky, A.; Perdew, J. P.; Csonka, G. I.; Vydrov, O. A.; Scuseria, G. E. Spurious fractional charge on dissociated atoms: Pervasive and resilient self-interaction error of common density functionals. *J. Chem. Phys.* **2006**, *125*, 194112.

- (20) Ruzsinszky, A.; Perdew, J. P.; Csonka, G. I.; Vydrov, O. A.; Scuseria, G. E. Density functionals that are one- and two- are not always

- many-electron self-interaction-free, as shown for  $\text{H}_2^+$ ,  $\text{He}_2^+$ ,  $\text{LiH}^+$ , and  $\text{Ne}_2^+$ . *J. Chem. Phys.* **2007**, *126*, 104102.
- (21) Cohen, A. J.; Mori-Sánchez, P.; Yang, W. Insights into current limitations of density functional theory. *Science* **2008**, *321*, 792–794.
- (22) Hait, D.; Head-Gordon, M. Delocalization errors in density functional theory are essentially quadratic in fractional occupation number. *J. Phys. Chem. Lett.* **2018**, *9*, 6280–6288.
- (23) Bryenton, K. R.; Adeleke, A. A.; Dale, S. G.; Johnson, E. R. Delocalization error: The greatest outstanding challenge in density-functional theory. *WIREs Comput. Mol. Sci.* **2022**, *13*, No. e1631.
- (24) Zhao, Y.; Lynch, B. J.; Truhlar, D. G. *J. Phys. Chem. A* **2004**, *108*, 2715–2719.
- (25) Perdew, J. P.; Zunger, A. Self-interaction correction to density-functional approximations for many-electron systems. *Phys. Rev. B* **1981**, *23*, 5048–5079.
- (26) Pederson, M. R.; Ruzsinszky, A.; Perdew, J. P. Communication: Self-interaction correction with unitary invariance in density functional theory. *J. Chem. Phys.* **2014**, *140*, 121103.
- (27) Langreth, D.; Perdew, J. The exchange-correlation energy of a metallic surface. *Solid State Commun.* **1975**, *17*, 1425–1429.
- (28) Gunnarsson, O.; Lundqvist, B. I. Exchange and correlation in atoms, molecules, and solids by the spin-density-functional formalism. *Phys. Rev. B* **1976**, *13*, 4274–4298.
- (29) Gunnarsson, O.; Lundqvist, B. I. Erratum: Exchange and correlation in atoms, molecules, and solids by the spin-density-functional formalism. *Phys. Rev. B* **1977**, *15*, 6006–6006.
- (30) Langreth, D. C.; Perdew, J. P. Exchange-correlation energy of a metallic surface: Wave-vector analysis. *Phys. Rev. B* **1977**, *15*, 2884–2901.
- (31) Becke, A. D. A new mixing of Hartree–Fock and local density-functional theories. *J. Chem. Phys.* **1993**, *98*, 1372–1377.
- (32) Görling, A.; Levy, M. Exact Kohn–Sham scheme based on perturbation theory. *Phys. Rev. A* **1994**, *50*, 196–204.
- (33) Levy, M. Universal variational functionals of electron densities, first-order density matrices, and natural spin-orbitals and solution of the  $v$ -representability problem. *Proc. Natl. Acad. Sci. U.S.A.* **1979**, *76*, 6062–6065.
- (34) Lieb, E. H. Density functionals for coulomb systems. *Int. J. Quantum Chem.* **1983**, *24*, 243–277.
- (35) Levy, M.; Perdew, J. P. Hellmann–Feynman, virial, and scaling requisites for the exact universal density functionals. shape of the correlation potential and diamagnetic susceptibility for atoms. *Phys. Rev. A* **1985**, *32*, 2010–2021.
- (36) Levy, M.; Perdew, J. P. *Single-Particle Density in Physics and Chemistry*; March, N. H.; Deb, B. M., Eds.; Academic: New York, 1987; pp. 54–55.
- (37) Yang, W. *Density Matrices and Density-Functionals*; Erdahl, R.; Smith, V. H., Jr., Eds.; Reidel: Dordrecht, Holland, 1987, p. 499.
- (38) Mori-Sánchez, P.; Cohen, A. J.; Yang, W. Self-interaction-free exchange-correlation functional for thermochemistry and kinetics. *J. Chem. Phys.* **2006**, *124*, No. 091102.
- (39) Kim, M.-C.; Sim, E.; Burke, K. Understanding and reducing errors in density functional calculations. *Phys. Rev. Lett.* **2013**, *111*, No. 073003.
- (40) Raghavachari, K.; Trucks, G. W.; Pople, J. A.; Head-Gordon, M. A fifth-order perturbation comparison of electron correlation theories. *Chem. Phys. Lett.* **1989**, *157*, 479–483.
- (41) Colonna, F.; Savin, A. Correlation energies for some two- and four-electron systems along the adiabatic connection in density functional theory. *J. Chem. Phys.* **1999**, *110*, 2828–2835.
- (42) Wu, Q.; Yang, W. A direct optimization method for calculating density functionals and exchange–correlation potentials from electron densities. *J. Chem. Phys.* **2003**, *118*, 2498–2509.
- (43) Teale, A. M.; Coriani, S.; Helgaker, T. The calculation of adiabatic-connection curves from full configuration-interaction densities: Two-electron systems. *J. Chem. Phys.* **2009**, *130*, 104111.
- (44) Teale, A. M.; Coriani, S.; Helgaker, T. Accurate calculation and modeling of the adiabatic connection in density functional theory. *J. Chem. Phys.* **2010**, *132*, 164115.
- (45) Yang, W.; Wu, Q. Direct method for optimized effective potentials in density-functional theory. *Phys. Rev. Lett.* **2002**, *89*, No. 143002.
- (46) Sala, F. D.; Görling, A. Efficient localized Hartree–Fock methods as effective exact-exchange Kohn–Sham methods for molecules. *J. Chem. Phys.* **2001**, *115*, 5718–5732.
- (47) Parr, R. G.; Yang, W. Density functional approach to the frontier-electron theory of chemical reactivity. *J. Am. Chem. Soc.* **1984**, *106*, 4049–4050.
- (48) Hou, L.; Irons, T. J. P.; Wang, Y.; Furness, J. W.; Wibowo-Teale, A. M.; Sun, J. Capturing the electron–electron cusp with the coupling-constant averaged exchange–correlation hole: A case study for Hooke’s atoms. *J. Chem. Phys.* **2024**, *160*, No. 014103.
- (49) Wu, Q.; Yang, W. Algebraic equation and iterative optimization for the optimized effective potential in density functional theory. *J. Theor. Comput. Chem.* **2003**, *02*, 627–638.
- (50) Császár, P.; Pulay, P. Geometry optimization by direct inversion in the iterative subspace. *J. Mol. Struct.* **1984**, *114*, 31–34.
- (51) *QUEST, a rapid development platform for QUantum electronic structure techniques*, <https://quest.codes/>, 2024.
- (52) Heaton-Burgess, T.; Bulat, F. A.; Yang, W. Optimized effective potentials in finite basis sets. *Phys. Rev. Lett.* **2007**, *98*, No. 256401.
- (53) Dunning, T. H. Gaussian basis sets for use in correlated molecular calculations. I. The atoms boron through neon and hydrogen. *J. Chem. Phys.* **1989**, *90*, 1007–1023.
- (54) Woon, D. E.; Dunning, T. H. Gaussian basis sets for use in correlated molecular calculations. III. The atoms aluminum through argon. *J. Chem. Phys.* **1993**, *98*, 1358–1371.
- (55) Woon, D. E.; Dunning, T. H. Gaussian basis sets for use in correlated molecular calculations. IV. Calculation of static electrical response properties. *J. Chem. Phys.* **1994**, *100*, 2975–2988.
- (56) Woon, D. E.; Dunning, T. H. Gaussian basis sets for use in correlated molecular calculations. V. Core-valence basis sets for boron through neon. *J. Chem. Phys.* **1995**, *103*, 4572–4585.
- (57) Helgaker, T.; Jørgensen, P.; Olsen, J. *Modern Electronic-Structure Theory*; Wiley: New York, 2000.
- (58) Helgaker, T.; Jørgensen, P. Configuration-interaction energy derivatives in a fully variational formulation. *Theor. Chim. Acta* **1989**, *75*, 111–127.
- (59) Helgaker, T.; Jørgensen, P. *Methods in Computational Molecular Physics*; Wilson, S.; Diercksen, G. H. F., Eds.; Plenum: New York, 1992; p. 353.
- (60) Reimann, S.; Borgoo, A.; Tellgren, E. I.; Teale, A. M.; Helgaker, T. Magnetic-field density-functional theory (BDFT): Lessons from the adiabatic connection. *J. Chem. Theory Comput.* **2017**, *13*, 4089–4100.
- (61) Lindh, R.; Malmqvist, P.-Å.; Gagliardi, L. Molecular integrals by numerical quadrature. I. radial integration. *Theor. Chem. Acc.* **2001**, *106*, 178–187.
- (62) Ekström, U.; Visscher, L.; Bast, R.; Thorvaldsen, A. J.; Ruud, K. Arbitrary-order density functional response theory from automatic differentiation. *J. Chem. Theory Comput.* **2010**, *6*, 1971–1980.
- (63) Lehtola, S.; Steigemann, C.; Oliveira, M. J.; Marques, M. A. Recent developments in libxc — a comprehensive library of functionals for density functional theory. *SoftwareX* **2018**, *7*, 1–5.
- (64) Dirac, P. A. M. Note on exchange phenomena in the Thomas atom. *Proc. Cam. Philos. Soc.* **1930**, *26*, 376–385.
- (65) Vosko, S. H.; Wilk, L.; Nusair, M. Accurate spin-dependent electron liquid correlation energies for local spin-density calculations—a critical analysis. *Can. J. Phys.* **1980**, *58*, 1200–1211.
- (66) Perdew, J. P.; Burke, K.; Ernzerhof, M. Generalized gradient approximation made simple. *Phys. Rev. Lett.* **1996**, *77*, 3865–3868.
- (67) Furness, J. W.; Kaplan, A. D.; Ning, J.; Perdew, J. P.; Sun, J. Accurate and numerically efficient r2SCAN meta-generalized gradient approximation. *J. Phys. Chem. Lett.* **2020**, *11*, 8208–8215.
- (68) Perdew, J. P. Jacob’s ladder of density functional approximations for the exchange-correlation energy. *AIP Conf. Proc.* **2001**, *577*, 1–20.
- (69) Sun, J.; Ruzsinszky, A.; Perdew, J. P. Strongly constrained and appropriately normed semilocal density functional. *Phys. Rev. Lett.* **2015**, *115*, No. 036402.

(70) Tao, J.; Perdew, J. P.; Staroverov, V. N.; Scuseria, G. E. Climbing the density functional ladder: Nonempirical meta-generalized gradient approximation designed for molecules and solids. *Phys. Rev. Lett.* **2003**, *91*, No. 146401.

(71) Zhao, Y.; Lynch, B. J.; Truhlar, D. G. Multi-coefficient extrapolated density functional theory for thermochemistry and thermochemical kinetics. *Phys. Chem. Chem. Phys.* **2005**, *7*, 43.

(72) Zhao, Y.; González-García, N.; Truhlar, D. G. Benchmark database of barrier heights for heavy atom transfer, nucleophilic substitution, association, and unimolecular reactions and its use to test theoretical methods. *J. Phys. Chem. A* **2005**, *109*, 2012–2018.

(73) Goerigk, L.; Grimme, S. A general database for main group thermochemistry, kinetics, and noncovalent interactions—assessment of common and reparameterized (meta-)GGA density functionals. *J. Chem. Theory Comput.* **2010**, *6*, 107–126.

(74) Goerigk, L.; Hansen, A.; Bauer, C.; Ehrlich, S.; Najibi, A.; Grimme, S. A look at the density functional theory zoo with the advanced GMTKN55 database for general main group thermochemistry, kinetics and noncovalent interactions. *Phys. Chem. Chem. Phys.* **2017**, *19*, 32184–32215.

(75) Karton, A.; Martin, J. M. L. Explicitly correlated w<sub>n</sub> theory: W1-f12 and W2-f12. *J. Chem. Phys.* **2012**, *136*, 124114.

(76) Kaplan, A. D.; Shahi, C.; Bhetwal, P.; Sah, R. K.; Perdew, J. P. Understanding density-driven errors for reaction barrier heights. *J. Chem. Theory Comput.* **2023**, *19*, 532–543.

(77) Kanungo, B.; Kaplan, A. D.; Shahi, C.; Gavini, V.; Perdew, J. P. Unconventional error cancellation explains the success of Hartree–Fock density functional theory for barrier heights. *J. Phys. Chem. Lett.* **2024**, *15*, 323–328.

(78) Hernandez, D. J.; Rettig, A.; Head-Gordon, M. A new view on density corrected DFT: Can one get a better answer for a good reason? *arXiv:2306.15016* **2023**, DOI: .

(79) Gill, P. M. W.; Johnson, B. G.; Pople, J. A.; Frisch, M. J. An investigation of the performance of a hybrid of Hartree–Fock and density functional theory. *Int. J. Quantum Chem.* **1992**, *44*, 319–331.

(80) Janesko, B. G.; Scuseria, G. E. Hartree–Fock orbitals significantly improve the reaction barrier heights predicted by semilocal density functionals. *J. Chem. Phys.* **2008**, *128*, 244112.

(81) Verma, P.; Perera, A.; Bartlett, R. J. Increasing the applicability of DFT I: Non-variational correlation corrections from hartree–fock dft for predicting transition states. *Chem. Phys. Lett.* **2012**, *524*, 10–15.

(82) Kim, M.-C.; Sim, E.; Burke, K. Ions in solution: Density corrected density functional theory (DC-DFT). *J. Chem. Phys.* **2014**, *140*, 18A528.

(83) Kim, M.-C.; Park, H.; Son, S.; Sim, E.; Burke, K. Improved DFT potential energy surfaces via improved densities. *J. Phys. Chem. Lett.* **2015**, *6*, 3802–3807.

(84) Sim, E.; Song, S.; Burke, K. Quantifying density errors in DFT. *J. Phys. Chem. Lett.* **2018**, *9*, 6385–6392.

(85) Vuckovic, S.; Song, S.; Kozłowski, J.; Sim, E.; Burke, K. Density functional analysis: The theory of density-corrected DFT. *J. Chem. Theory Comput.* **2019**, *15*, 6636–6646.

(86) Santra, G.; Martin, J. M. What types of chemical problems benefit from density-corrected DFT? a probe using an extensive and chemically diverse test suite. *J. Chem. Theory Comput.* **2021**, *17*, 1368–1379.

(87) Sim, E.; Song, S.; Vuckovic, S.; Burke, K. Improving results by improving densities: Density-corrected density functional theory. *J. Am. Chem. Soc.* **2022**, *144*, 6625–6639.

(88) Teale, A. M.; Coriani, S.; Helgaker, T. Range-dependent adiabatic connections. *J. Chem. Phys.* **2010**, *133*, 164112.

(89) Dass, K. J.; Grossi, J.; Vuckovic, S.; et al. Large coupling-strength expansion of the Møller–Plesset adiabatic connection: From paradigmatic cases to variational expressions for the leading terms. *J. Chem. Phys.* **2020**, *153*, 214112.